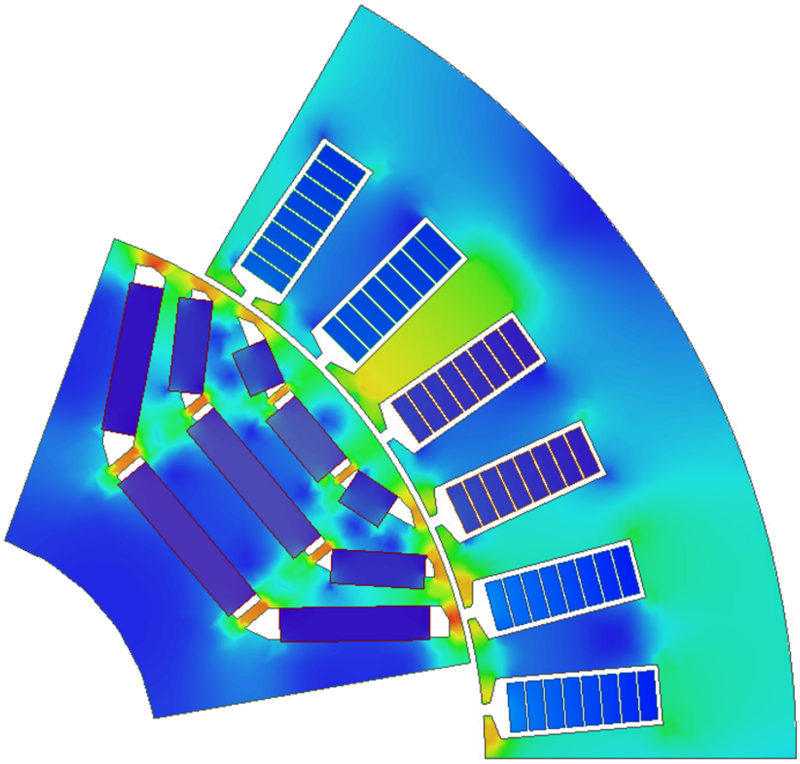

Comparison of a highly sustainable PMaSynRM with a traditional PMSM

Performance and environmental analysis of a PMaSynRM with ferrite magnets and aluminium hairpin winding compared to a PMSM with NdFeB magnets and copper round-wire winding

Master's thesis in Master Programmes:
Sustainable Electric Power Engineering and Electromobility
Systems, Control and Mechatronics

Anton Ingemansson, Elias Kambrin

Department of Electrical Engineering
CHALMERS UNIVERSITY OF TECHNOLOGY
Gothenburg, Sweden 2022

Master's thesis 2022

Comparison of a highly sustainable PMaSynRM with a traditional PMSM

Performance and environmental analysis of a PMaSynRM with ferrite magnets and aluminium hairpin winding compared to a PMSM with NdFeB magnets and copper round-wire winding

Anton Ingemansson
Elias Kambrin

Department of Electrical Engineering
Division of Electric Power Engineering
Chalmers University of Technology
Gothenburg, Sweden 2022

Comparison of a highly sustainable PMaSynRM with a traditional PMSM
Performance and environmental analysis of a PMaSynRM with ferrite magnets and aluminium hairpin winding compared to a PMSM with NdFeB magnets and copper round-wire winding
ANTON INGEMANSSON
ELIAS KAMBRIN

Supervisor: Elisabet Jansson, Volvo Car Corporation
Examiner: Torbjörn Thiringer, Department of Electrical Engineering

Master's Thesis 2022
Department of Electrical Engineering
Division of Electric Power Engineering
Chalmers University of Technology
SE-412 96 Gothenburg
Telephone +46 31 772 1000

Gothenburg, Sweden 2022

Comparison of a highly sustainable PMaSynRM with a traditional PMSM
Performance and environmental analysis of a PMaSynRM with ferrite magnets and aluminium hairpin winding compared to a PMSM with NdFeB magnets and copper round-wire winding
ANTON INGEMANSSON
ELIAS KAMBRIN
Department of Electrical Engineering
Chalmers University of Technology

Abstract

In this thesis, a PMaSynRM with ferrite magnets and aluminium hairpin winding was designed and compared to a reference PMSM with Nd(Dy)FeB magnets and copper round-wire winding, for vehicle application. The design and simulation of the PMaSynRM was done in Ansys Electronics and it consisted of a parametric optimisation of the rotor structure for improved performance. The performance requirements of the vehicle included a top speed of 150 km/h, an acceleration from 0-100 km/h in 10 s, and to complete the WLTP and CADC 150 drive cycles. For this evaluation, a vehicle dynamics model was created based on the parameters for the Volvo C30 electric car model. Further, an MTPA controller was created in Matlab to find the operating region of the motor and to map the losses through interpolation. A simplified model of the powertrain was created in Simulink to calculate the energy consumption and required torque of the motor for the WLTP and CADC 150 drive cycles. It was found that the PMaSynRM and reference motor had an acceleration from 0-100 km/h in 9.72 s and 9.82 s respectively and that they could both handle the WLTP and CADC 150 drive cycles. The loss of energy for the PMaSynRM and reference motor was compared for the two drive cycles. It was found that the aluminium hairpin winding had lower winding losses than the copper round-wire, despite the frequency dependency of the phase resistance due to eddy current effects in the hairpin winding. Further improvements were seen with lower hysteresis and eddy current losses due to the lower flux density from the ferrite magnets compared to the Nd(Dy)FeB magnets in the reference motor. However, the PMaSynRM has a limited operating region due to the risk of demagnetization of the ferrite magnets which reduces the performance.

An environmental and cost analysis was conducted for the two motors to investigate the impact of the different materials. The environmental impact was measured with the EPS system, which aims to preserve the natural capital, and is measured in the economic value of ELU. It was found that the PMaSynRM had a 96.1 % lower total impact in ELU compared to the reference motor. Most notable, the aluminium hairpin winding had a 99.9 % lower environmental impact compared to the copper round-wire winding. Further, the total cost in USD of the PMaSynRM was found to be 77.0 % lower than the reference motor.

Keywords: PMaSynRM, PMSM, ferrite, hairpin, aluminium, copper, environmental impact, ELU, GWP.

Acknowledgements

We would like to thank Volvo Car Corporation and the whole of the Electric Machine Design team for giving us the opportunity to do our Master's thesis with them. We are especially grateful for all the support and feedback during the whole project from our supervisor Elisabet Jansson and examiner Torbjörn Thiringer.

Anton Ingemansson & Elias Kambrin
Gothenburg, June 2022

Abbreviations

BEV	Battery Electric Vehicle
CADC	Common Artemis Drive Cycle
CO	Carbon Oxide
CO_2	Carbon Oxide
CO_2-eq	Carbon Dioxide equivalent
ELU	Environmental Load Unit
EPS	Environmental Priority Strategies
GWP	Global Warming Potential
HC	Hydro Carbons
HEV	Hybrid Electric Vehicle
LCA	Life Cycle Analysis
MTPA	Maximum Torque Per Ampere
Nd(Dy)FeB	Neodymium-Dysprosium-Iron-Boron
NEDC	New European Driving Cycle
NO_x	Carbon Oxide
PM	Permanent magnet
PMaSynRM	Permanent Magnet Assisted Synchronous Reluctance Machine
PMSM	Permanent Magnet Synchronous Machine
SynRM	Synchronous Reluctance Machine
WLTP	Worldwide harmonised Light vehicle Test Procedure

Nomenclature

α	Slope angle
β	Current angle between i_s and i_d
δ	Air gap length
η	Steinmetz or Hysteresis constant
μ_0	Permeability of vacuum
ξ	Reduced conductor height
ρ	Resistivity
ρ_{air}	Density of air
σ	Electrical conductivity
$\psi_{d,q}$	d- and q-axis flux linkage
ψ_{PM}	Magnet flux linkage
Ω_{rpm}	Mechanical rotational speed
ω_{motor}	Angular velocity of the motor
ω_r	Electrical angular velocity of the motor
ω_{wheel}	Angular velocity of the wheels
A_{cond}	Area of a conductor
A_f	Cross sectional area of the car
a	Acceleration
B_{max}	Maximum flux density
B_r	Residual magnetic flux density
b_{cond}	Conductor width
b_{slot}	Slot width
C_d	Aerodynamic drag coefficient
C_r	Rolling resistance coefficient
E_{input}	Motor input energy
E_{output}	Motor output energy
E_{wheel}	Wheel energy
F_{acc}	Acceleration force
F_{aero}	Aerodynamic force
F_{grad}	Gradient force
$F_{retractive}$	Sum of all the retractive forces
F_{roll}	Rolling resistance force
$F_{tractive}$	Sum of all the tractive forces
F_{wheel}	Wheel force

f	Electrical frequency
g	Gravitational constant
H_c	Coercive force
h_{cond}	Conductor height
h_{end}	Height of end winding
I_{max}^{rms}	Maximum current in rms
ID_{stator}	Inner stator diameter
i_{abc}	3-Phase current
$i_{d,q}$	d- and q-axis current
i_s	Stator current
$i_{s,max}$	Maximum stator current
J_{max}^{rms}	Maximum current density in rms
K_e	Material specific eddy current loss coefficient
k_{fill}	Conductor fill factor of a slot
k_R	Average resistance factor for the conductors in a slot
$k_{R,k}$	Resistance factor for the kth winding layer
$L_{d,q}$	d- and q-axis stator inductance
l_{coil}	Length of one turn
l_{end}	Length of end winding
l_{total}	Total length of a conductor
m_{car}	Mass of the car
$N_{parallel}$	Number of parallel branches
$N_{periods}$	Number of electrical periods
N_{steps}	Number of steps per electrical periods
n_{step}	Step size of the mechanical rotational speed
OD_{stator}	Outer stator diameter
P_{AC}	AC winding losses
P_{core}	Core loss
P_{DC}	DC winding losses
P_{eddy}	Eddy current loss
P_{hyst}	Hysteresis loss
P_{input}	Motor input power
P_{max}	Maximum power
P_{output}	Motor output power
P_{solid}	Solid loss
$P_{stranded}$	Stranded loss
P_{wheel}	Power on the wheels
p	Number of pole pairs
q	Number of slots per pole
R_{AC}	Stator phase AC resistance
R_{DC}	Stator phase DC resistance
r	Number of conductors per slot
r_s	Stator phase resistance
r_t	Gear ratio
r_{wheel}	Radius of the wheels
T_{max}	Maximum torque

T_{output}	Motor output torque
T_{step}	Torque step
T_{wheel}	Torque on the wheels
t	Core lamination thickness
t_{step}	Step time
t_{stop}	Stop time
$u_{d,q}$	Steady state d- and q-axis voltage
u_s	Stator voltage
$u_{s,max}$	Maximum stator voltage
V	Volume of the magnetic material
v_{car}	Velocity of the car
v_{wind}	Velocity of the wind

Contents

1

Introduction

The demand for battery electric vehicles (BEV) and hybrid electric vehicles (HEV) has increased rapidly in recent years since they are more efficient and less polluting than traditional combustion engine vehicles powered by non-renewable sources [1]. The emissions from a combustion engine contains carbon dioxide (CO2), which contributes to global warming, and the toxic gases carbon oxide (CO), hydrocarbons (HC), nitrogen oxides (NOx). Electric vehicles have the potential to be more sustainable and many traditional car manufacturers are reorganising to only manufacture HEVs and BEVs. As an example, Volvo Cars are aiming to only produce fully electric cars by 2030 [2].

For traction drive systems in electric vehicles, the permanent magnet synchronous machine (PMSM) utilising rare-earth Neodymium-Iron-Boron (NdFeB) magnets are typically used [3]. However, the cost of mining such rare materials is very high due to supplies being scarce and highly localised to a few places in the world [4]. The current recycling rate of rare-earth elements is also very low. The need for rare-earth-free permanents magnets (PM) to be used in electric propulsion applications is thus growing. An alternative to the NdFeB magnets is to use ferrites, which have a lower environmental impact during manufacturing and a substantially lower material cost [5][6][7]. However, ferrite magnets have a lower magnetic flux density than NdFeB magnets, leading to a decreased output torque when used in a PMSM [8]. A possible option is to use a permanent magnet assisted synchronous reluctance machine (PMaSynRM). It uses the structure of a synchronous reluctance machine (SynRM) with added magnets in the flux-barriers, which utilises the reluctance torque of the SynRM and the magnetic torque of the magnets to increase the total torque.

Different materials have different environmental impact. A study conducted by [7], compared the environmental impact, measured in Environmental Load Unit (ELU), of a PMSM with NdFeB magnets to a PMaSynRM with ferrite magnets. The study showed that the PMSM had a 5.2 % larger environmental impact during the production phase. Another possibly important material change for the environmental aspect is replacing the stator winding material from copper to aluminium. The environmental impact, measured in ELU, is 131 for copper but only 0.16 for aluminium [9]. The main reason for the big difference is the resource amount, with aluminium being the third most common material in the earth's crust. The environmental impact could be further reduced by changing the stator winding from round-wire to hairpin, which could improve the performance of the motor [10]. The hairpin winding has lower DC losses, but the AC losses are larger due to skin and proximity effect. This means that for high-speed applications the winding losses will increase compared to the round-wire winding. However, by changing to aluminium winding that effect could be dampened due to the lower conductivity. Aluminium has larger DC losses but more importantly, it has less AC losses than copper [9]. Aluminium is also cheaper than copper, 3,500 USD/tons compared to 10,000 USD/tons [11].

1.1 Previous work

Several investigations of replacing NdFeB magnets with ferrites have been conducted previously. One study investigated two different rotor structures for a six pole PMaSynRM with round-wire copper stator winding [12]. The spoke type rotor and the arc-type with both three and four layers were analysed. A PMSM NdFeB motor was used as a reference. The study showed that only the four-layer arc-type rotor could match the reference motor, but also that the three-layer reaches just a slightly lower performance with lower magnet volume. The analysed geometrical parameters of the arc-type rotor were the middle flux-barrier width and thickness, the position of the flux-barriers, and the side flux-barrier width and thickness. The magnet size was changed along with the flux-barrier measurement changes. A similar study, where an investigation of the influence of the flux-barrier design on the torque and torque ripple was conducted in [13]. In contrast to [12], the focus was only on a three-layer arc-type rotor with four poles without ferrite magnets in the side flux-barriers. The thickness and angle of the side flux-barriers, the position of the barriers, and the width of the magnet-filled middle flux-barrier were analysed. The magnet to flux-barrier ratio was kept constant and not analysed in that report either. The main focus of the analysis was on the torque and torque ripple, but also the saliency and flux linkage. Further investigations can be done by investigating the impact of side magnets and the magnet to flux-barrier ratio.

In both reports, the traditional copper round-wire stator winding was used. A study by [14] compared the round-wire winding to hairpin winding. The latter has higher losses at high frequencies, due to the proximity effect, but lower losses at low frequencies due to the larger area of the conductor. The round-wire conductors minimise the proximity effect since they are divided into many wires with a small area. However, by increasing the number of conductors, the hairpin winding achieves a similar loss characteristic as the round-wire winding. The study compared two, four, and eight conductors per slot. It showed that, during speeds up to 20,000 rpm, eight conductors per slot have less copper losses than the round-wire winding.

The impact of the slot opening size was also investigated by [14]. A smaller slot opening gives less leakage flux and lower losses, however, if it is completely closed the leakage flux will increase. The study investigated different sizes from closed to open with steps of 20 %, with the openings centered in the middle. It found that 20 % was the best slot opening. The position of the conductors also affects the losses, with 43 % of the winding losses at high speed is located in the first conductor. To minimise that loss the conductors should be placed with minimum distance to each other and the stator yoke. This will create a bigger gap between the stator slot opening and the first conductor, which decreases the winding losses.

In [9], the difference between using aluminium and copper as a material for the hairpin winding was investigated. The study showed that the winding losses of aluminium are lower at high frequencies and higher at low frequencies compared to copper. This suggests that aluminium hairpin winding compensates for the drawbacks of the traditional copper hairpin winding as highlighted in [14]. In the study by [9], it was shown that the aluminium hairpin is comparable to the copper hairpin, in terms of performance and efficiency, while also being more sustainable and cheaper.

Another aspect to consider when designing an electric motor is demagnetisation of the magnets. This was investigated by [15], where a six-pole rotor with ferrite magnets were used. The study showed that the first layer of magnets, closest to the air gap, is the most exposed to demagnetisation. It also showed that the risk could be minimised with thicker magnets in that layer. When all layers had equal thickness, 40 % of the magnet in the first layer became demagnetised. However, by keeping the same total amount of magnet but redistributing it to get a thicker magnet in the first layer, the demagnetisation was reduced to about 12 % of the magnet. To reduce the amount further, tapered ends could be used on the flux-barriers. This increases the flux flow close to the tangential rib, since the steel area increases. However, this also has a negative impact on the output power in the high-speed region.

1.2 Problem description

This thesis compares a PMSM using NdFeB magnets and copper round wire windings with a PMaSynRM using ferrite magnets and aluminium hairpin windings, for automotive purpose. The motor should be mounted in a city car and handle an acceleration from 0-100 km/h in 10 seconds, have a top speed of 150 km/h and handle the WLTP-3 and CADC 150 drive cycles. A physical model of the car is designed in Simulink to calculate the required torque from the motor, in order to handle the drive cycles, acceleration and top speed requirements. A PMSM which can handle the same requirements is used as a reference motor. The goal is to design a motor that meets the requirements but is cheaper and more sustainable than the reference motor. This is done by optimising the PMaSynRM to minimise the amount of material used.

The motor is designed in Ansys Electronics. It consists of designing the hairpin winding to meet the requirements of current density and the performance characteristics. The stator is then created to fit the hairpin windings. The next step is to create the rotor, while the stator is kept fixed. The rotor is created with an initial setup, from previous reports, and then improved with a parametric optimisation. In the optimisation the rotor variables are examined to find an improved design.

To evaluate the efficiency of the PMaSynRM to the reference motor a simplified model of the powertrain is built in Simulink. The two motors are tested for the WLTP-3 and CADC 150 drive cycles to investigate the energy consumption on a realistic driving pattern.

2

Theory

This chapter presents the most important concepts and necessary theoretical background needed to understand the rest of the report.

2.1 Vehicle Dynamics

A vehicle in motion is under the influence of different force, both working with the car and against it, see Fig 2.1. The force required to accelerate the vehicle is described by Newtons second law of motion

$$F_{acc} = m_{car}\, a \tag{2.1}$$

where a is the acceleration and m_{car} is the mass of the vehicle. The magnitude and direction of that force is the difference between the sum of the tractive forces, $F_{tractive}$, and the sum of the retractive forces, $F_{retractive}$, as given by

$$F_{acc} = F_{tractive} - F_{retractive} \tag{2.2}$$

If the resulting force is positive, the vehicle accelerates in its forward direction. If the force instead is negative, the vehicle is either accelerating in its reverse direction or decelerating in its forward direction.

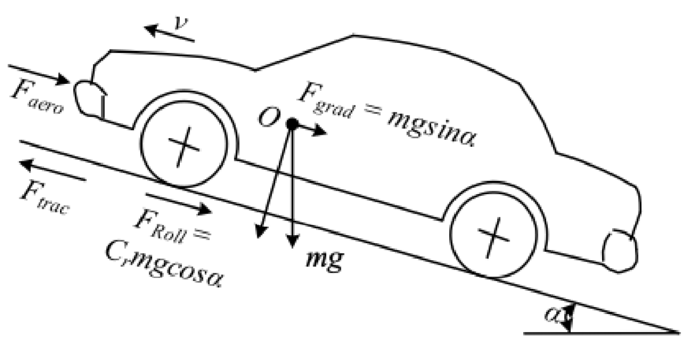

Figure 2.1: Image of the forces acting on a car while driving [16].

2.1.1 Tractive Forces

Tractive forces are forces working to move a vehicle in the intended direction. For a car there are two tractive forces. The first and major one is F_{wheel}, which is the force put to the wheels by the motor, through the gears and the drive shaft. The second force, F_{grad}, appears when the road is elevated. When driving downhill,i.e. negative incline angle α, the gravity makes F_{grad} a tractive force. When driving uphill F_{grad} instead becomes a retractive force. F_{grad} is defined as a retractive force, which can be seen in Fig 2.1. The tractive force is simply described by

$$F_{tractive} = F_{wheel} = F_{acc} + F_{retractive} \tag{2.3}$$

As can be seen, in order to achieve a certain F_{acc}, F_{wheel} needs to compensate for the retractive forces.

2.1.2 Retractive Forces

The retractive forces that influence the vehicle comes from aerodynamic drag F_{aero}, rolling resistance F_{roll}, and the gravitational force F_{grad}, and is given by

$$F_{retractive} = F_{aero} + F_{grad} + F_{roll} \tag{2.4}$$

where F_{aero} is the force from the aerodynamic drag, dependent on the vehicle velocity and defined as

$$F_{aero} = \frac{1}{2}\,\rho_{air}\,C_d\,A_f\,(v_{car} - v_{wind})^2 \tag{2.5}$$

where ρ_{air} (kg/m^3) is the density of air, the dimensionless C_d is the aerodynamic drag coefficient, A_f (m^2) is the cross sectional area of the car, v_{car} (m/s^2) and v_{wind} (m/s^2) is the velocity of the car and wind respectively. The direction of v_{wind} is defined as the intended direction of the car. F_{grad} is described by and described by

$$F_{grad} = m_{car}\,g\sin(\alpha) \tag{2.6}$$

where g is the gravitational constant and α is the incline angle of the hill. The last retractive force, F_{roll}, is defined by

$$F_{roll} = C_r\,g\,m_{car}\cos(\alpha) \tag{2.7}$$

where C_r is the rolling resistance coefficient.

2.1.3 Wheel power and torque

The power put to the wheels from the motor is calculated trough

$$P_{wheel} = F_{wheel}\, v_{car} \tag{2.8}$$

From that equation, together with the angular velocity of the wheel, given by

$$\omega_{wheel} = \frac{2\pi}{\frac{2\pi\, r_{wheel}}{v_{car}}} = \frac{v_{car}}{r_{wheel}} \tag{2.9}$$

where r_{wheel} is the radius of the wheel. Further, the wheel torque can be calculated with

$$T_{wheel} = \frac{P_{wheel}}{\omega_{wheel}} \tag{2.10}$$

To calculate the torque from the motor the gear ratio, r_t, needs to be considered. The gear ratio creates a difference in rotational speed between the electric motor and the wheels [17], and is a constant and selected value. The gear ratio affects the angular velocity according to

$$\omega_{motor} = r_t\, \omega_{wheel} \tag{2.11}$$

This will in turn affect the torque in a similar way since the power output from the motor and the power put to the wheels are the same and therefore

$$T_{motor} = \frac{P_{output}}{\omega_{motor}} = \frac{1}{r_t}\frac{P_{wheel}}{\omega_{wheel}} = \frac{T_{wheel}}{r_t} \tag{2.12}$$

2.2 Electrical and mechanical constraints

This section presents both electrical and mechanical constraints that have to be taken into account in the design of a rotating electric machine.

2.2.1 Current density

The current density in a winding is an important factor in electric motor design, as the resistive losses of the winding is proportional to the square of the current density. The resistive losses are also proportional to the stator phase resistance r_s which in turn is proportional to the resistivity and the area of the conductor. Further, the temperature difference between the teeth and the conductors is proportional to the resistive losses. The allowed loading level for a motor is therefore dependent on the insulation around the winding as well as the cooling of the motor. In [18], a table with empirical values can be found that provides an indication of the maximum allowable rms value for the current density depending on the motor and cooling type. For a non-salient pole synchronous machine with direct water cooling, the permitted current density $J = 7 - 10$ A/mm^2 for continuous operation, assuming copper windings. The maximum current density in a coil can be calculated using

$$J_{max}^{rms} = \frac{I_{max}^{rms}}{N_{parallel} A_{cond}} \tag{2.13}$$

where $N_{parallel}$ is the number of parallel branches and A_{cond} is the area of each individual conductor and I_{max}^{rms} is the maximum current in rms.

2.2.2 Air gap length

In a synchronous machine magnetised by permanent magnets, the air gap length is selected based on mechanical constraints [18]. The physical air gap length between the stator and rotor is an important factor of the characteristics and performance of the motor. For a PMSM, the air gap length is generally very small so as to reduce the amount of magnet material or to increase the output torque of the motor. However, a small air gap increase the eddy current losses on the surface of the stator and rotor. Furthermore, the current harmonics of the stator causes increased rotor surface losses due to the smaller air gap. Lastly, the magnets could reach a high temperature due to losses caused by harmonics in the air gap at higher speeds. The allowed air gap length of a PMSM can be estimated empirically using

$$\delta = \frac{0.18 + 0.006 P_{output}^{0.4}}{1000} \tag{2.14}$$

where δ is the air gap length in meters and P_{output} is the output power in Watts.

2.3 MTPA

Maximum Torque Per Ampere (MTPA) is a control strategy that minimises the stator current while maintaining the required torque of the motor. It aims to minimise the resistive losses of the winding. A boundary condition is obtained from the voltage and current amplitude limit that gives the safe operating region of the motor. The voltage limit and the current limit are the two constraints of MTPA and the operating point should be within these limits.

2.3.1 Torque calculation using MTPA

The output torque of a PMSM can be calculated using flux linkages and currents in d- and q-axis according to

$$T_{output} = \frac{3p}{2}(\psi_d i_q - \psi_q i_d) \tag{2.15}$$

where p is the number of pole pairs, ψ_d and ψ_q are the stator flux linkages in dq-coordinates. i_d and i_q are the stator currents in dq-coordinates. By using that $\psi_d = \psi_{PM} + L_d i_d$ and $\psi_q = L_q i_q$, (2.15) can be divided into torque from the permanent magnets and reluctance torque as

$$T_{output} = \frac{3p}{2}\psi_{PM} i_q + \frac{3p}{2}(L_d - L_q) i_d i_q \tag{2.16}$$

where ψ_{PM} is the flux linkage in d-axis created by the permanent magnets. L_d and L_q are the stator inductance in d- and q-axis and are defined as

$$L_q = \frac{\psi_q}{i_q} \tag{2.17}$$

$$L_d = \frac{\psi_d - \psi_{PM}}{i_d} \tag{2.18}$$

The electromagnetic torque of a PMSM is a function of i_d and i_q as shown in (2.16). By using the definition of d- and q-axis current

$$i_d = i_s \cos(\beta) \tag{2.19}$$

$$i_q = i_s \sin(\beta) \tag{2.20}$$

where β is the angle between the stator current i_s and the d-axis, (2.16) can be derived as

$$T_{output} = \frac{3p}{2}\left[\psi_{PM} i_s \sin(\beta) + (L_d - L_q)\frac{\sin(2\beta)}{2} i_s^2\right] \tag{2.21}$$

where it can be seen that the torque is also depending on the current angle β. The maximum produced torque is then found by differentiating the torque with respect to β which gives

$$\frac{dT_{output}}{d\beta} = \frac{3p}{2}\left[\psi_{PM} i_s \cos(\beta) + (L_d - L_q) i_s^2 \cos(2\beta)\right] \tag{2.22}$$

It can then be derived that the optimal current angle that results in maximum torque per ampere is

$$\beta = \cos^{-1}\left(\frac{-\psi_{PM} \pm \sqrt{\psi_{PM}^2 + 8(L_d - L_q)^2 i_s^2}}{4(L_d - L_q)i_s}\right) \tag{2.23}$$

2.3.2 Current limit

The stator current i_s can be described in the dq-coordinate system as

$$i_s = \sqrt{i_d^2 + i_q^2} \tag{2.24}$$

If a maximum stator current $i_{s,max}$ is given, then the d and q-axis current is limited to the circle defined by

$$i_{s,max} \geq \sqrt{i_d^2 + i_q^2} \tag{2.25}$$

2.3.3 Voltage limit

For a PMSM the voltage limit can be derived using the steady state d- and q-axis voltage definitions as

$$u_d = r_s i_d - \omega_r \psi_q = r_s i_d - \omega_r L_q i_q \tag{2.26}$$

$$u_q = r_s i_q + \omega_r \psi_d = r_s i_q + \omega_r L_d i_d + \omega_r \psi_{PM} \tag{2.27}$$

where $\psi_d = L_d i_d + \psi_{PM}$ and $\psi_q = L_q i_q$. The stator voltage u_s can then be derived as

$$u_s^2 = u_d^2 + u_q^2 = (r_s i_d - \omega_r L_q i_q)^2 + (r_s i_q + \omega_r L_d i_d + \omega_r \psi_{PM})^2 \tag{2.28}$$

by neglecting the voltage drop of the stator winding resistance, (2.28) can be expressed as

$$\frac{u_s^2}{\omega_r^2} = (L_d i_d + \psi_{PM})^2 + (L_q i_q)^2 \tag{2.29}$$

$$\frac{(i_d + \frac{\psi_{PM}}{L_d})^2}{\frac{u_s^2}{\omega_r^2 L_d^2}} + \frac{i_q^2}{\frac{u_s^2}{w_r^2 Lq^2}} = 1 \tag{2.30}$$

Finally, for a maximum voltage $u_{s,max}$ the voltage limit is obtained in the form of an ellipse expressed as

$$\frac{(i_d + \frac{\psi_{PM}}{L_d})^2}{L_q^2} + \frac{i_q^2}{L_d^2} \leq \left(\frac{u_{s,max}}{\omega_r L_d L_q}\right)^2 \tag{2.31}$$

As can be seen in (2.31), the voltage ellipse will decrease in size towards its center as the rotor speed ω_r increases.

2.4 Losses

The losses of a rotating electrical motor has a significant impact on the performance and feasibility of the motor. The losses include both mechanical and electrical losses, the latter commonly divided into winding and iron losses. The iron losses, or core losses, mainly consist of eddy current, hysteresis, and stray losses. In this section, the eddy current, hysteresis, and winding losses are introduced.

2.4.1 Eddy current losses

Eddy currents are circulating currents induced by a perpendicular alternating magnetic field. Eddy currents occur in electromagnetic materials such as conductors or the core lamination. The magnitude of the eddy currents are proportional to the area of the closed loop of circulating currents. Hence, the core of an electric motor is made up of a large number of thin sheets of electrical steel with an insulating material in between. The losses caused by eddy currents in a magnetic material can be expressed by

$$P_{eddy} = k_e B_m^2 t^2 f^2 V \tag{2.32}$$

where k_e is a material specific coefficient found for eddy current losses, B_m is the magnitude of the flux density, t is the thickness of the core lamination, f is the electrical frequency, and V is the volume of the magnetic material.

2.4.2 Hysteresis losses

A magnetic field across a magnetic material causes the molecules to align with the direction of the field. When a time-varying magnetic field is applied, the direction of the field is periodically reversed. The internal friction of the molecules inside the magnetic material opposes the magnetic force from the time-varying magnetic field. This causes a loss of energy in the form of heat and is called hysteresis loss. The hysteresis losses of a magnetic material can be expressed in terms of power loss according to Bertotti's equation

$$P_{hyst} = k_h B_m^2 f \tag{2.33}$$

where k_h is the coefficient for hysteresis loss.

2.4.3 Winding losses

Winding losses is the result of joule heating caused by electrical currents in the conductors of stator windings. In the case of uniform current distribution and a 3-phase connection, the winding losses are given by

$$P_{DC} = 3R_{DC}I_{rms}^2 \tag{2.34}$$

where R_{dc} is the DC phase resistance of the winding, as given by

$$R_{dc} = \rho\frac{l_{total}}{A_{cond}N_{parallel}} \tag{2.35}$$

where l_{total} and A_{cond} is the total length and cross-sectional area of the conductor in a coil, ρ is the resistivity of the conductor material, and $N_{parallel}$ is the number of parallel paths of the windings per phase. For a stator winding arrangement with hairpin conductors, (2.35) can be derived by taking into account the number of turns as

$$R_{dc} = \rho\frac{l_{coil}}{A_{cond}} \cdot \frac{r \cdot q \cdot p}{N_{parallel}^2} \tag{2.36}$$

where l_{coil} is the length of one turn, r is the number of conductors per slot, q is the number of slots per pole, and p is the number of poles.

2.4.3.1 Influence of eddy current effects on conductors

When an alternating current is passing through a conductor it creates an alternating flux in the material, which has a substantial impact on the resistance. This is due to eddy effects which includes both skin effect and proximity effect occurring in the conductor. These effects are frequency dependent and cause a non-uniform current distribution inside and amongst the conductors which decreases the effective cross-sectional area of the conductors, leading to higher losses. Skin effect is explained by the resulting alternating magnetic field created by the alternating current which induces opposing eddy currents inside the conductor. With increasing frequency the current flow moves closer to the surface of the conductor and the current density decreases exponentially towards the center of the conductor. Proximity effect is caused by two or more conductors in close proximity to each other. It is the result of the alternating magnetic field created around a conductor when an alternating current is flowing through it, which leads to eddy currents being induced in nearby conductors. The resulting current distribution of conductors in close proximity of each other is then altered, leading to an increased current density away from the adjacent conductors in the case of currents of the same polarity.

In [18] an analytical model is presented to calculate the increased losses caused by the frequency dependent eddy effects, which it refers to as the AC resistance or losses. It defines a factor k_R as the ratio between AC and DC resistances of the conductor, which can be multiplied to the DC winding losses to get the AC winding losses. For a rectangular conductor the reduced area caused by skin effect is regarded as a reduced conductor height defined as

$$\xi = h_{cond}\sqrt{\frac{1}{2}\omega_r\mu_0\sigma\frac{b_{cond}}{b_{slot}}} \tag{2.37}$$

where h_{cond} and b_{cond} is the conductor height and width, b_{slot} is the slot width, ω is the electrical angular frequency, μ_0 is the vacuum permeability, and σ is the electrical conductivity of the conductor material. For a slot with r number of winding layers, the resistance factor for the kth layer is

$$k_{R,k} = \varphi(\xi) + k(k-1)\psi(\xi) \tag{2.38}$$

where increasing winding layer k corresponds to conductors closer to the slot opening. Further, $\varphi(\xi)$ and $\psi(\xi)$ are functions of the reduced conductor height and are defined as

$$\varphi(\xi) = \xi\frac{\sinh(2\xi) + \sin(2\xi)}{\cosh(2\xi) - \cos(2\xi)} \tag{2.39}$$

followed by

$$\psi(\xi) = 2\xi\frac{\sinh(\xi) - \sin(\xi)}{\cosh(\xi) + \cos(\xi)} \tag{2.40}$$

As seen in (2.38) the resistance factor increases with the layer number, with the top layer being closest to the slot opening. Assuming series-connected conductors, the average resistance factor of a slot is

$$k_R = \varphi(\xi) + \frac{r^2 - 1}{3}\psi(\xi) \tag{2.41}$$

An effective way to reduce the impact of eddy currents in conductors and thereby reducing the resistance factor is to introduce parallel-connected conductors. Circulating currents must then be prevented in the connections of the parallel branches by ensuring that the leakage flux is the same for each parallel-connected branch. This is achieved by transposition in the end winding of the parallel-connected conductors.

2.5 Demagnetisation

Demagnetisation can occur when a magnet is exposed to a strong surrounding magnetic field that counteracts the internal magnetic field of the magnet [15]. Fig. 2.2 shows the demagnetisation curve. The demagnetisation occurs when the flux density of the magnet reaches the knee point. Beyond this point, the region of irreversible demagnetisation starts [19]. The maximum flux density will thereby decrease, as illustrated by the red dashed line in Fig. 2.2. The amount of demagnetisation in the magnet depends on how far into the region the magnet is pushed, by the surrounding field [15]. Once the magnet becomes fully demagnetised it will stop working completely.

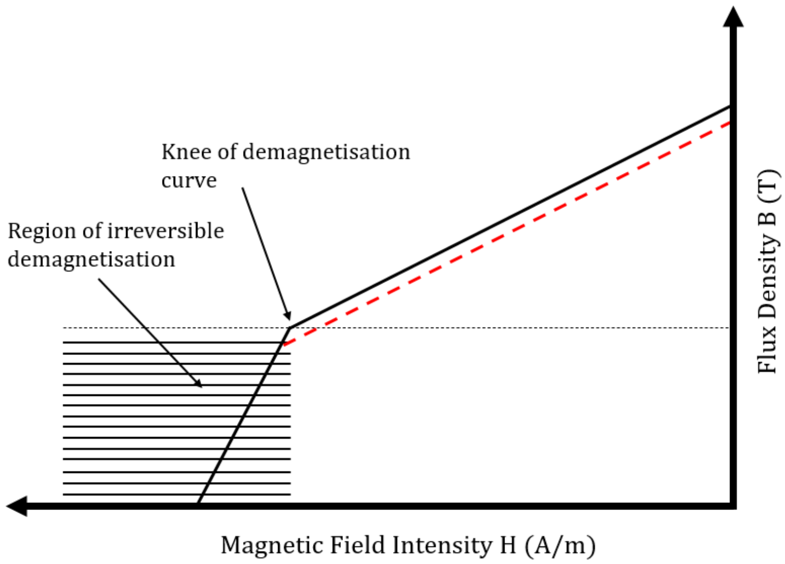

Figure 2.2: Demagnetisation curve.

3

Sizing and Requirements

An electric motor has both constraints and different types of requirements, depending on the purpose of the motor. It can be both performance related as well as physical and electrical limitations. The performance requirements of this thesis are presented in this chapter together with the parameters of the chosen vehicle model, the electrical constraints and a description of a benchmark motor.

3.1 Vehicle parameters

To analyse the efficiency of the motor, a vehicle model was specified. Due to the limited performance of a ferrite PMaSynRM, it is beneficial to have a smaller and lighter vehicle. It was also beneficial to select a car that was already electric, since the additional weight of the batteries and other electrical components are taken into account. A compromise between the city and highway car defined in [20], was selected and it was specified to have the characteristics of the Volvo C30 electric, depicted in Fig. 3.1. The characteristics of the car are presented in Table 3.1 [20]. Most BEVs of a similar size have a maximum motor speed of 10,000 - 12,000 rpm and the maximum speed for this study was therefore chosen as 12,000 rpm. The values in Table 3.1 were used together with the equations in Section 2.1 to calculate the vehicle dynamics of the selected car.

Table 3.1: Volvo C30 electric Parameters.

	Variable	Value
Curb Weight	m_{car}	1,725 kg
Density of Air	ρ_{air}	1.225 kg/m^3
Frontal Area	A_d	2.18 m^2
Rolling Resistance Coefficient	C_r	0.0098
Wheel Radius	r_{wheel}	0.26 m

Figure 3.1: Volvo C30 electric.

3.2 Performance requirements

The aim was to create an electric motor that can be used to power the desired vehicle model. The top speed requirement was set to 150 km/h and the acceleration time from 0-100 km/h was set to 10 seconds. With a top speed of 150 km/h and a desired motor speed of 12,000 rpm, the gear ratio was set to 7.78. From this an acceleration pattern was created, see Fig. 3.2a. In order to translate the pattern into the required torque and power, the vehicle dynamics equations in Section 2.1 was used, which resulted in the torque-speed and power curve seen in Fig. 3.2b. It is assumed that the acceleration requirement define the required maximum torque from the motor. The motor in the car should also handle some common drive cycles. The motor was tested on the drive cycles Worldwide harmonised Light vehicle Test Procedures (WLTP) and Common Artemis Drive Cycle (CADC).

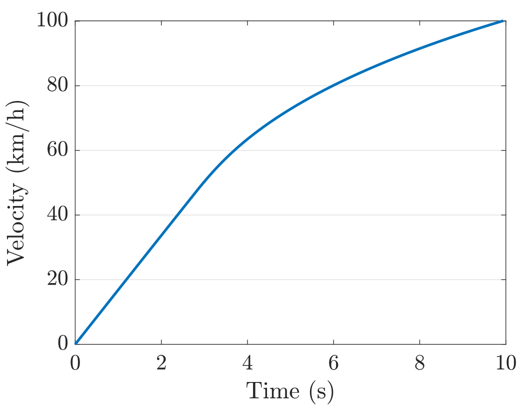

(a) 0-100 km/h acceleration.

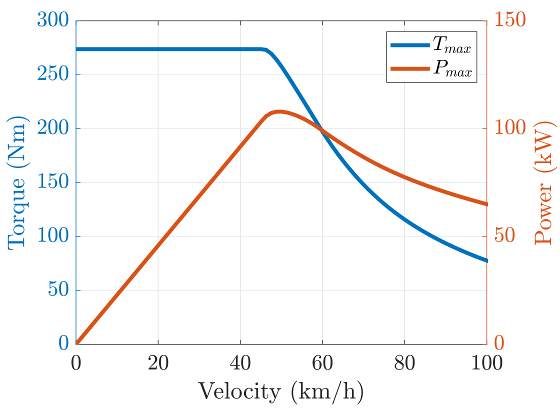

(b) Torque-speed and power curve.

Figure 3.2: Acceleration pattern and resulting maximum torque and power curves.

3.2.1 WLTP

WLTP is a test made on a car with a dynamometer to determine the emissions and fuel consumption [21]. For an electric car it also determines the range [22]. WLTP is the latest procedure used for type approval testing of light-duty vehicles, e.g. passenger cars [21]. Between 2017-2019 it replaced the old procedure, New European Driving Cycle (NEDC) which was designed in the 1980s and had become outdated due to development in technology [22]. WLTP was developed with real driving data collected with the help from many different countries. The new drive cycle was designed to give a more realistic estimation of driving patterns. WLTP cycle has three different classes, made to simulate different types of vehicles and the driving characteristics from different countries [21]. The drive cycle used in this study was the WLTP class 3b, since the vehicle is assumed to suit the European market and have a maximum velocity above 120 km/h. The class 3b drive cycle is shown in Fig. 3.3a, and as can be seen it consists of four sections, low, middle, high and extra high. The corresponding torque requirements from the motor during the drive cycle is shown in Fig. 3.3b.

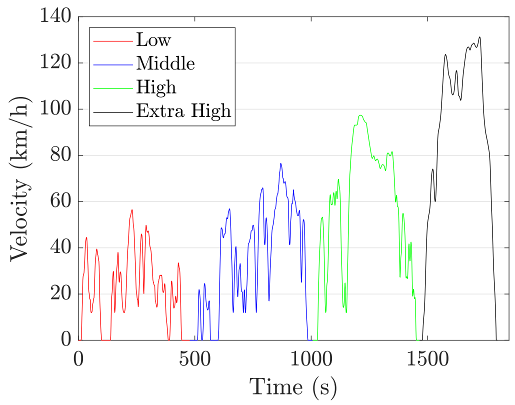

(a) Velocity-time curve.

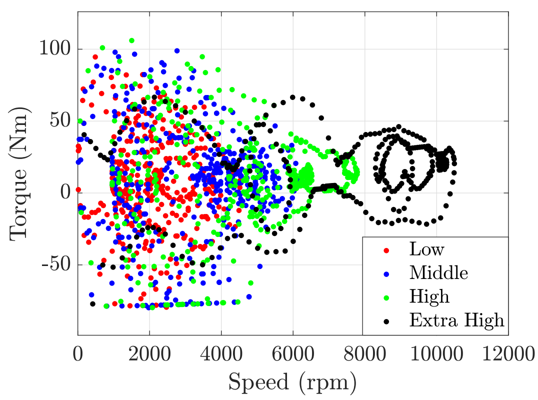

(b) Torque-Speed plot.

Figure 3.3: WLTP Drive Cycle.

3.2.2 CADC

The CADC is a drive cycle that, similar to WLTP, has been designed from real driving patterns [23]. CADC has focused on data from vehicles operated in normal traffic. The drive cycle is depicted in Fig. 3.4a and is divided into three different parts urban, road and motorway traffic. The motorway part has two versions, maximum speed of 130 km/h or 150 km/h, but since the top speed of the car was set to 150 km/h only the 150 km/h version was used. Fig 3.4b shows the torque requirements of the car during the drive cycle.

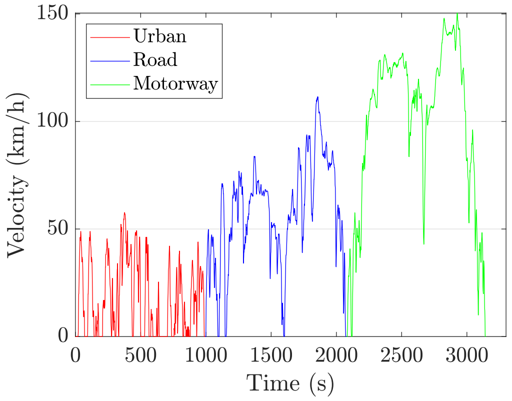

(a) Velocity-time curve.

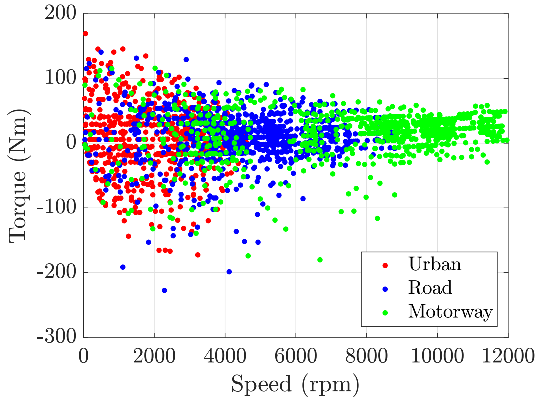

(b) Torque-Speed plot.

Figure 3.4: CADC 150 Drive Cycle.

3.3 Road Load

Road load is the combined retractive force from the rolling resistance F_{roll} (2.7) and aerodynamic drag, F_{aero} (2.5), described in Section 2.1.2. Road load is mainly determined by the aerodynamic drag since it increases with the square of the velocity, as can be seen in (2.5). The road load increases exponentially as the velocity increases, which is depicted in Fig. 3.5. It increases until it intersects with the maximum torque-speed curve, which determines a theoretical top speed of the car. As Fig. 3.5 shows, the required output torque from the motor at 150 km/h or 12,000 rpm is 27 Nm.

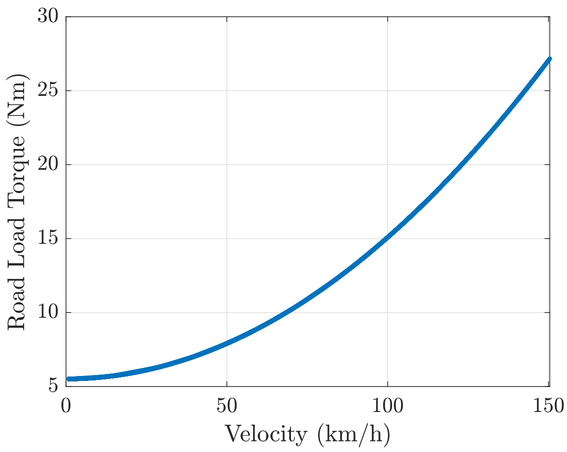

Figure 3.5: Road load for the car for different velocities.

3.4 Electrical constraints

The voltage and current supply to the motor depends on the battery and inverter model respectively. In this study the battery and inverter models are neglected.

Commercial, non sport, BEVs usually have a DC voltage level of around 300 - 400 V [20]. For the intended vehicle model in this study, the voltage limit was chosen to 400V. The maximum allowed current was defined in [20] as 233 and 468 A rms for a city and highway car respectively. Since the vehicle model in this thesis has a performance requirement similar to a compromise between the two cars, the current limit was chosen as 350 A rms.

3.5 PMSM reference motor

As a benchmark, a reference PMSM motor as depicted in Fig. 3.6 was used. It is a motor that has previously been used as a reference motor by [24]. The rotor was inspired by the Chevrolet Bolt BEV and the stator was inspired by the Volvo XC90 HEV. The length and diameter of the motor was scaled to fulfill the requirements specified in Section 3.2. Further, the electrical constraints as described in Section 3.4 were used. The motor has four magnets divided into two layers and uses short pitched round-wire winding. The motor parameters are presented in Table 3.2. Further, the materials used for the reference motor are specified in Table 3.3. The steel material was changed to the same material that will be used for the PMaSynRM.

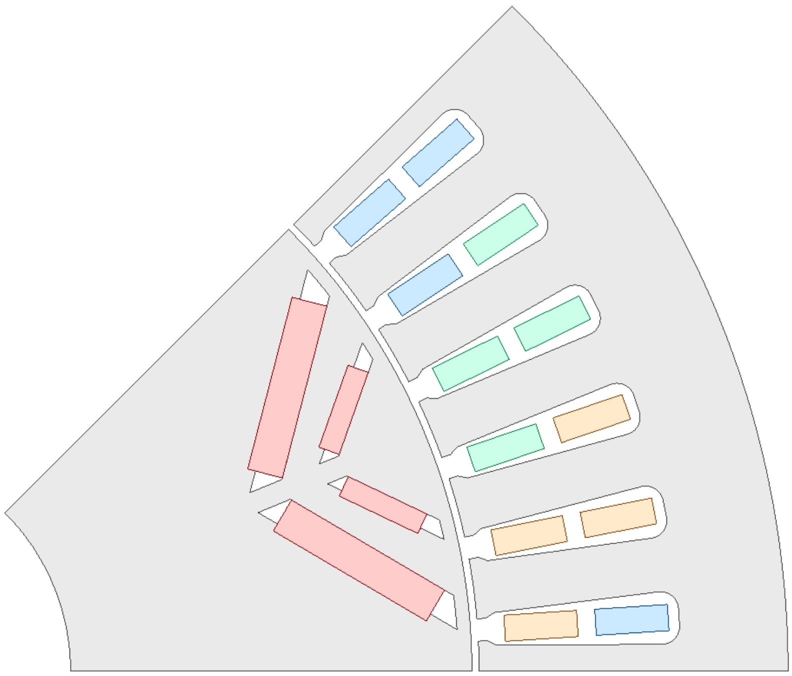

Figure 3.6: Geometry of the reference motor.

Table 3.2: Reference motor parameters.

Peak power	130 kW
Maximum torque	170 Nm
Time to 100 km/h	9.82 s
Base speed	6,500 rpm
Maximum speed	12,000 rpm
Gear ratio	7.78
DC Voltage	400 V
Maximum current (RMS)	350 A
DC resistance	11.1 mΩ
Slot fill factor	45 %
Number of poles	8
Number of slots	48
Stator outer diameter	210 mm
Rotor outer diameter	139.5 mm
Stack length	105 mm
Air gap width	0.8 mm

Table 3.3: Reference motor material specification.

Part	Material	Material specification
Winding	Copper	Appendix A.1
Magnets	Nd(Dy)FeB	Appendix A.2
Rotor	M19_29G	Appendix A.3
Stator	M19_29G	Appendix A.3

4

Design and Parametric Optimisation of the Motor Structure using FEM Software

The design of a motor is done in several different steps and in this chapter the design phase of the motor is presented. An initial design of the motor geometry was designed based on previous work and optimised to meet the performance requirements of this study, with regards to minimising the material amount in the motor.

4.1 Initial rotor geometry

In the design of the rotor geometry, a literature study was conducted to aid the selection of the initial parameters. One study investigated the suitable number of poles for a PMaSynRM using ferrite magnets in order to achieve high power and torque [15]. The results from this study indicated that the 6-pole motor is optimal for producing a high amount of torque and output power for low-speed operation, while the 4-pole model exhibited higher output power for high-speed operation. Due to the requirements specified in Section 3.2, a 6-pole machine was chosen. The geometry of the rotor for the PMaSynRM can be seen in Fig. 4.1a which shows one pole of the 6-pole rotor as well as the variables for the flux-barrier and magnets. These variables are used in the parametric optimisation of the rotor, as described further in Section 4.4. In Fig. 4.1b the parameter names for the mechanically supporting ribs as well as the air gap next to the central magnets are shown. These parameters have a fixed value to limit the number of parameters for the parametric optimisation, thereby reducing the simulation time. A description of all parameters for the rotor geometry is presented in Table 4.1. The inner and outer diameter of the rotor is 60 and 143 mm respectively and the material is defined as electrical steel of type M19_29G. More information about the steel lamination material for the rotor can be found in Appendix A.3. As for the selection of ferrite material, magnets of grade FB9B were chosen. The material properties of the FB9B magnets have been obtained from the supplier TDK, see Appendix A.4 [25].

An optimised design of the rotor geometry is important to achieve a good performance. The main objective is to obtain a high torque and power density, while

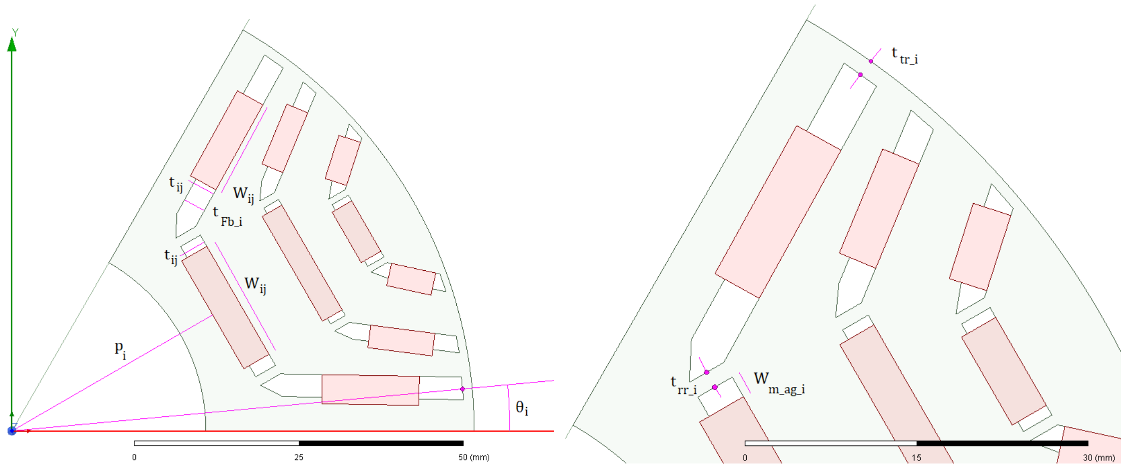

(a) Variables. **(b)** Fixed parameters.

Figure 4.1: PMaSynRM rotor structure and geometric variables.

Table 4.1: Rotor Geometry Description.

Description	Variable
Magnet Position	p_i
Magnet Width	W_{ij}
Magnet Thickness	t_{ij}
Flux-barrier Angle	Θ_i
Flux-barrier Thickness	t_{Fb_i}
Tangential rib thickness	t_{tr_i}
Radial rib thickness	t_{rr_i}
Magnet Air gap Width	$W_{m\_ag\_i}$

Index $i = 1, 2, 3$ indicates the flux-barrier layer while $j = 1, 2$ indicates the central or side magnets respectively.

keeping the torque ripple low. For the initial design of the PMaSynRM, a paper investigating the influence of the flux-barrier design on the torque and torque ripple was taken into consideration [13]. The investigated parameters include the magnet position and width as well as the flux-barrier thickness and angle. A sensitivity analysis was conducted in the study based on performance indicators including torque, torque ripple, flux linkage from the magnets, and saliency. It was found that the flux-barrier angle has a significant effect on the torque ripple. Further, the magnet position greatly affects the saliency and output torque, while the magnet width influences the PM flux linkage. The study also suggested that the flux-barrier thickness has a smaller effect on the performance indicators [13]. The study performed an optimisation of the geometrical parameters to find a compromise between torque and minimum torque ripple and these results have been taken into consideration for the initial design of the PMaSynRM in this report. In order to enhance the flux density in the air gap and to achieve a higher output torque, magnets were also placed inside the angled flux-barriers on both sides of the central magnets. These magnets have the same thickness as the central magnets for each corresponding flux-barrier layer. The width of these magnets are selected so that the size can easily be varied as will be described in Section 4.4.

For ease of fabrication and mechanical support, ribs or bridges that connect the flux-barriers are necessary. In the rotor design of this study, both tangential and radial ribs are present. These increase the leakage flux in the rotor and become highly saturated when the flux level is high. As stated in [26], a thinner rib gives improved saliency but decreases the mechanical strength of the rotor. Further, one study states that the minimum thickness of ribs is $1 - 1.5$ mm with regards to the mechanical constraints [27]. For the intended rotor design of this study, it was assumed that such a thickness is sufficient for the operating range of the motor. As the flux-barrier closest to the rotor shaft has the highest mechanical stress, the rib thickness for this layer is the largest followed by the second and third layer. The values of the tangential and radial rib thicknesses is indicated in Table 4.2. As for the air gap next to the central magnets, it is assumed that the optimal design is to let the magnets fill up as much of the central flux-barrier as possible. The magnet air gap width was therefore set and fixed to 1 mm, which reduces the number of variables for the parametric optimisation.

In [15], a demagnetisation analysis was conducted to investigate the influence of the demagnetising field at low temperatures. The study consisted of determining the demagnetisation coefficient of different rotor designs in order of reducing the risk of irreversible demagnetisation while maintaining a high output torque. The study found that the magnets closest to the air gap have the highest demagnetisation coefficient. The proposed solution to this is to increase the thickness of the magnets closer to the surface of the rotor. The study also showed that the demagnetisation coefficient could be further decreased by implementing a tapered shape to the flux-barrier at the tangential ribs. With all this taken into consideration, the initial design of the rotor was constructed, as illustrated in Fig. 4.2, and the initial geometrical parameters are found in Table 4.2.

Table 4.2: Rotor Initial Geometrical Parameters.

Variable		Barrier, i = 1	Barrier, i = 2	Barrier, i = 3
p_i	(mm)	35.86	50.08	59.78
$W_{i,1}$	(mm)	19.23	18.67	9
$W_{i,2}$	(mm)	16	10	5
$t_{i,1}$	(mm)	4	4	4.3
$t_{i,2}$	(mm)	4	4	4.3
Θ_i	(deg)	5.39	10.95	18.93
t_{Fb_i}	(mm)	3.5	2.5	2.5
t_{tr_i}	(mm)	1.5	1.25	1
t_{rr_i}	(mm)	1.5	1.25	1
$W_{m\_ag\_i}$	(mm)	1	1	1

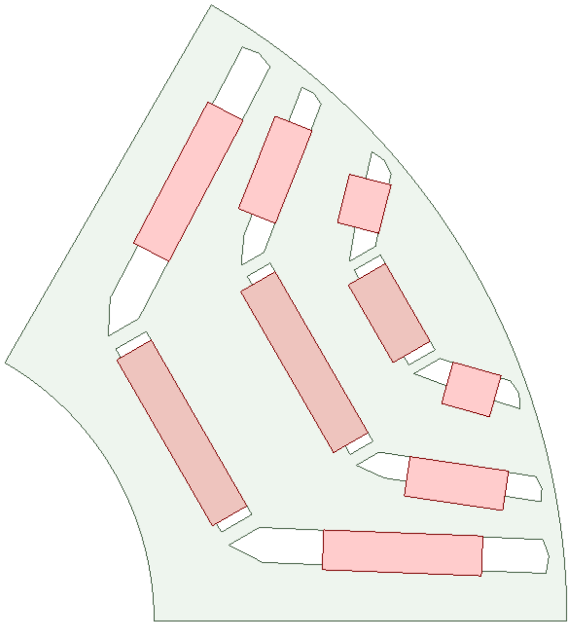

Figure 4.2: Initial rotor design.

4.2 Initial stator geometry

The stator dimensions are based on a theoretical optimal diameter ratio of the inner and outer diameter of the stator [18], and is given by

$$\frac{ID_{stator}}{OD_{stator}} = 0.6 \tag{4.1}$$

where ID_{stator} and OD_{stator} are the inner and outer diameter of the stator respectively. The inner diameter of the stator was calculated from the outer diameter of the rotor and the mechanically constrained air gap length as determined by (2.14). Assuming an output power of 108 kW, which is the analytical maximum power as presented in Section 3.2, the air gap length $\delta = 0.8$ mm. This air gap length was chosen to account for the mechanical limitations and high losses of a small air gap at higher speeds. The inner diameter of the stator then becomes 144.6 mm and the outer stator diameter was determined using (4.1) and set to 240 mm. The geometry of the stator together with the rotor and the hairpin winding can be seen in Fig. 4.3a.

The stator slots are of a rectangular shape to fit the hairpin winding, and the geometry of the stator slots can be seen in Fig. 4.3b together with the corresponding geometrical parameters. A description of the parameters, including their values, can be found in Table 4.3. The area of the stator slot was determined based on the electrical constraints described in Section 2.2.1, which helps to determine the size of the hairpin conductors, as will be shown in Section 4.3. It was assumed that the slot fill factor for the hairpin winding $k_{fill} = 65$ %. The slot width and height were investigated for the given slot area to achieve a high output torque. The slot opening width w_{so} is also an important factor in that it impacts the leakage flux and thereby the loss distribution of the hairpin winding. It was determined based on a study that found that a slot opening of 20 % of the slot width results in high output torque while keeping the torque ripple and resistance ratio R_{AC}/R_{DC} low [14]. Finally, the material used for the stator lamination is defined as M19_29G electrical steel, see Appendix A.3.

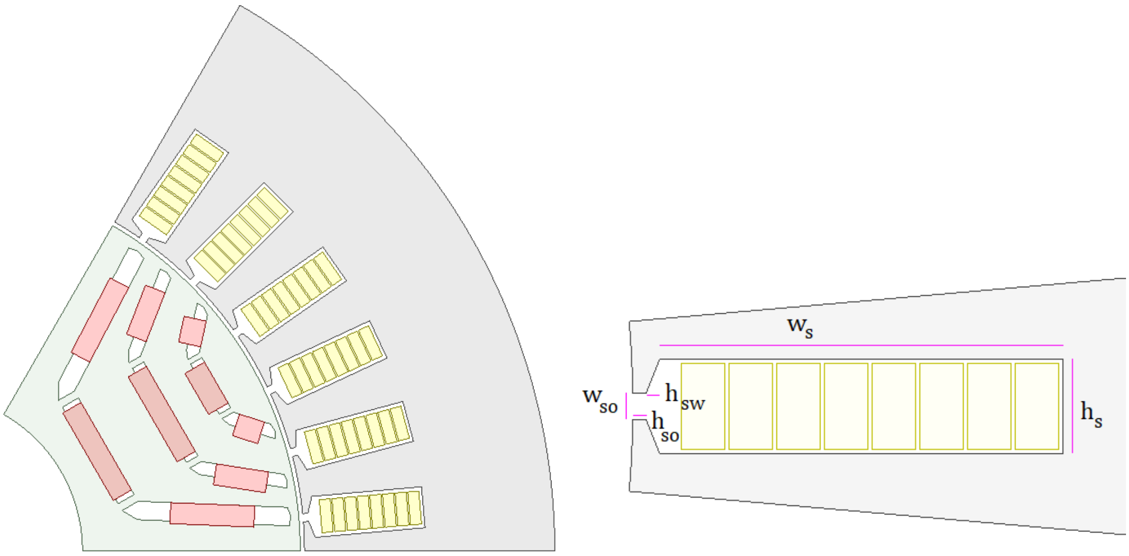

(a) Initial stator design. **(b)** Stator slot geometry.

Figure 4.3: Geometry of the stator and stator slots.

Table 4.3: Stator Slot Geometrical Parameters.

Description	Variable	Value
Slot height	h_s	21 mm
Slot width	w_s	7.83 mm
Slot opening height	h_{so}	1 mm
Slot wedge height	h_{sw}	1 mm
Slot opening width	w_{so}	1.57 mm

4.3 Hairpin winding geometry

For the initial design of the winding arrangement, several previous works were investigated and initial testing was conducted to reach a performance similar to the set requirements. One study found that a higher number of winding layers or conductors per slot, resulted in an increase of resistive losses due to the decreased area of each individual coil [14]. However, it also leads to a decrease of the AC loss component because of lower eddy losses caused by skin effect. This means that for high speed motors, a higher number of winding layers could result in lower overall losses of the motor. Both six and eight conductors per slot were investigated and finally eight conductors per slot was chosen as it resulted in the desired performance of this study. The study conducted in [14] also indicated that the losses could be further reduced if the distance between conductors is minimised and if they are placed close to the yoke. The material used for the hairpin winding is aluminium instead of copper, which is traditionally used for the stator winding. Aluminium has a higher resistivity than copper which leads to an increase of DC losses. On the contrary, the higher resistivity leads to a reduction of the AC losses in the winding caused by skin and proximity effect, which is highly prevalent in hairpin winding [9]. The full specification of the conductor material can be found in Appendix A.5. The geometry of the hairpin winding can be seen in Fig. 4.4 and the corresponding geometrical parameters are further described and presented in Table 4.4.

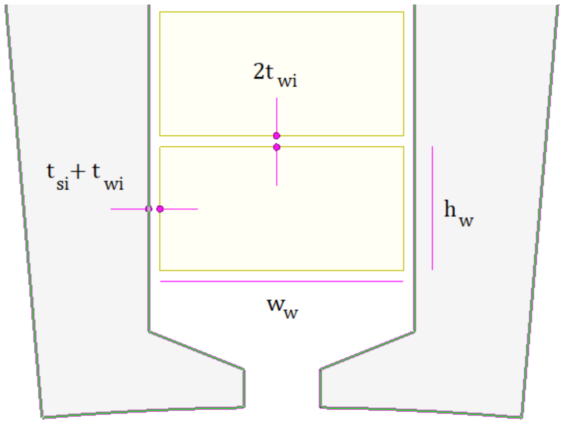

Figure 4.4: Geometrical parameters of the hairpin winding.

Table 4.4: Hairpin Winding Geometrical Parameters.

Description	Variable	Value
Wire width	w_w	6.31 mm
Wire height	h_w	2.12 mm
Wire insulation thickness	t_{wi}	0.15 mm
Slot insulation thickness	t_{si}	0.49 mm

The wire width and height were determined based on the required area to fulfil the constraint on current density described in Section 2.2.1. In electric motor applications, maximum current is only applied for a short period of time, i.e. during acceleration. Therefore, a larger current density limit can be assumed. For copper winding it is assumed that a maximum current density $J_{max}^{rms} = 20$ A/mm^2 is permitted. The maximum current density will however be lower for aluminium stator winding. By assuming that the DC losses of aluminium stator winding should be equal to the DC losses of copper winding, the ratio between required aluminium and copper conductor area can be calculated using (2.34)-(2.36). From this, it is achieved that the maximum permitted current density for aluminium winding $J_{max}^{rms} = 13.1$ A/mm^2 and the conductor area $A_{cond} = 13.36$ mm^2.

The insulation thickness around each wire and the insulation thickness around the slot was obtained from a study investigating the lifetime of insulation of a electric motor with hairpin winding [28]. A slightly larger insulation thickness was chosen in this report to account for the large mechanical stress that significantly reduces the lifetime of the insulation. The insulation material is modelled as empty space in Ansys Electronics while the conductors are set as solid conductors in order to evaluate the impact of current distribution in the conductor. Further, the conductors are connected in series with two parallel branches.

4.3.1 Phase resistance calculation

The DC phase resistance of the hairpin winding was calculated using (2.36). The length of one coil was determined by the length of the motor and by assuming that the average length of the end winding can be calculated as

$$l_{end} = 2\sqrt{\left(\frac{ID_{stator}/2 + h_{so} + h_{sw} + w_s/2}{2} \cdot \frac{2\pi}{6}\right)^2 + h_{end}^2} \tag{4.2}$$

where h_{end} is the height or length of the end winding that extends out from the stator and is assumed to be equal to 30 mm. The length of one coil then equals

$$l_{coil} = 2(l_{motor} + l_{end}) \tag{4.3}$$

and the path of the coil is depicted in Fig. 4.5. For the intended motor with aluminium hairpin winding, $r = 8$, $q = 2$, $p = 3$, $N_{parallel} = 2$, and $l_{motor} = 150$ mm, the phase DC resistance becomes $R_{DC} = 12$ mΩ. After changes to the length of motor, as will be described in Section 4.5.2, $l_{motor} = 100$ mm resulting in $R_{DC} = 9.8$ mΩ.

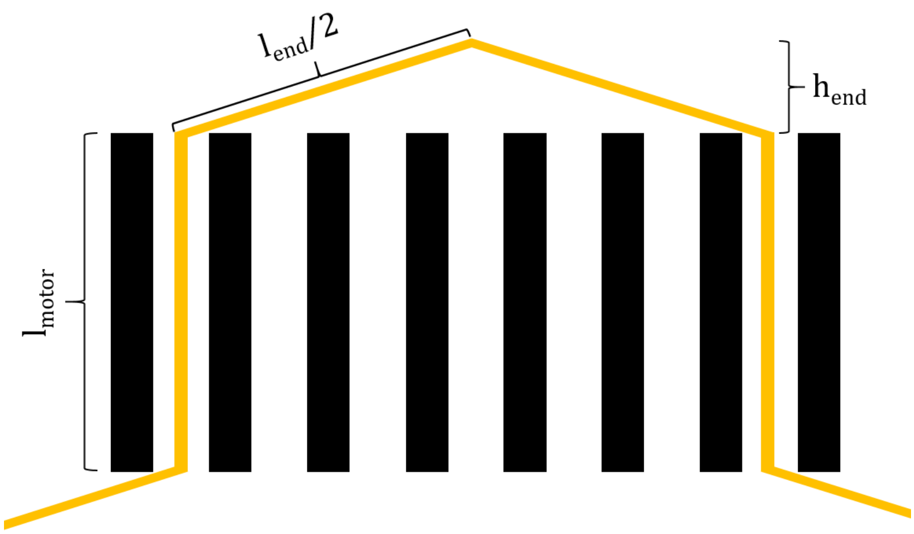

Figure 4.5: The path of one hairpin coil.

4.4 Parametric optimisation of the rotor

A parametric optimisation of the rotor variables described in Table 4.5 was done to improve the performance of the motor. The performance indicators that were examined are described in Table 4.6. The table also presents the results for the initial rotor and the improved rotor, the geometry of which will be described in Section 4.4.1. The analysis in Ansys Electronics was done with a full load study at one operating point and an optimetric sweep of the dq-currents. The operating point of the full load study was obtained through the MTPA analysis of the initial motor design. The MTPA controller will be described further in Section 6.1. From this, the base speed, maximum stator current and corresponding current angle β was taken as input for the full load study of the parametric optimisation. As for the optimetric study, an MTPA analysis was done to process the results from Ansys Electronics.

Table 4.5: Rotor Variables.

Description	Variable
Magnet Position	p_i
Magnet Width	W_{ij}
Magnet Thickness	t_{ij}
Flux-barrier Angle	Θ_i
Flux-barrier Thickness	t_{Fb_i}

Index $i = 1, 2, 3$ indicates the flux-barrier layer while
$j = 1, 2$ indicates the central or side magnets respectively.

Table 4.6: Performance Indicators for the parametric optimisation.

Analysis	Description	Unit	Initial rotor	Improved rotor	Difference
Full load	Average torque	(Nm)	254.3	281.9	+10.9 %
	Torque ripple	(%)	30.2	24.1	-20.2 %
Optimetric	Base speed	(rpm)	3,500	3,700	+5.7 %
	Maximum torque	(Nm)	255.5	283.7	+11.0 %
	Torque at 8000 rpm	(Nm)	63.8	95.3	+49.4 %
	Torque at 12000 rpm	(Nm)	33.4	50.1	+50.0 %
	Time to 100 km/h	(s)	11.83	8.83	-25.4 %
	$T_{magnetic}/T_{reluctance}$	(%)	15.84	23.9	+50.9 %
	Maximum power	(kW)	97.8	116.5	+19.1 %

The parametric optimisation was done by alternating the rotor variables by an initial change of ±10 % from their original values. By examining the results from the full load and optimetric study, the optimal variable value was chosen. This was an iterative process of taking the optimal value by changing the variables one at a time and continuously updating the rotor geometry, with regards to mechanical constraints. It was assumed that a distance of 1.5 mm between flux-barriers was sufficient. The optimisation was done two times in parallel, one in the order of the variables presented in Table 4.5 and the other in the reverse order. This was done since the change of a variable affects another. The aim was to increase the torque and power of the motor to minimise the time to 100 km/h, while keeping the torque ripple low. The time to 100 km/h was chosen as a good performance indicator, since it takes into account a large part of the operating region and not only the maximum torque.

4.4.1 Improved Rotor Geometry

The parametric optimisation, resulted in an improved rotor design where the magnets have been increased in both length and width. The barriers have been moved closer to the air gap, and the side barrier angles, θ_i, have been reduced. Fig. 4.6 depicts the improved rotor design, which can be compared to the initial rotor design in Fig. 4.2. The geometrical parameters of the improved rotor are presented in Table 4.7 together with the respective change for each variable compared to the initial rotor presented in Table 4.2

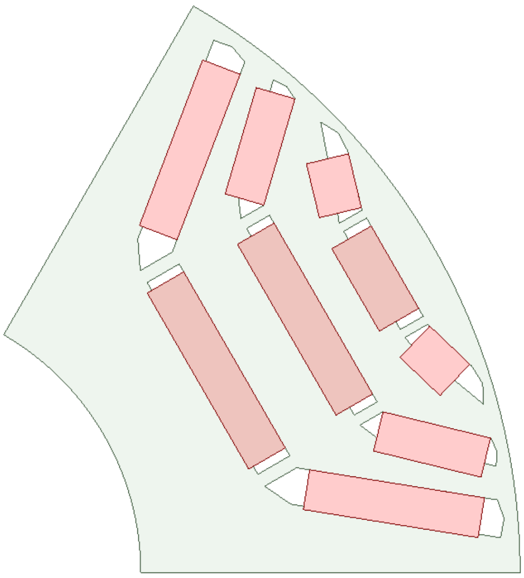

Figure 4.6: Improved rotor design.

Table 4.7: Geometrical parameters of the improved rotor.

Variable	Unit	Barrier, i = 1		Barrier, i = 2		Barrier, i = 3	
p_i	(mm)	41.86	+16.7%	53.08	+6.0%	61.78	+3.3%
$W_{i,1}$	(mm)	22.21	+15.5%	21.56	+15.5%	10.40	+15.6%
$W_{i,2}$	(mm)	17.36	+8.5%	10.10	+1.0%	6.05	+21.0%
$t_{i,1}$	(mm)	4.62	+15.5%	4.62	+15.5%	4.97	+15.6%
$t_{i,2}$	(mm)	4.40	+10.0%	4.40	+10.0%	4.73	+10.0%
Θ_i	(deg)	4.85	-10.0%	10.86	-0.8%	17.04	-10.0%
t_{Fb_i}	(mm)	4.04	+15.4%	2.89	+15.6%	2.89	+15.6%
t_{tr_i}	(mm)	1.50	0.0%	1.25	0.0%	1.00	0.0%
t_{rr_i}	(mm)	1.50	0.0%	1.25	0.0%	1.00	0.0%
$W_{m\_ag\_i}$	(mm)	1.00	0.0%	1.00	0.0%	1.00	0.0%

4.5 Size adjustment of the motor

In order to make a fair comparison between the reference motor and the PMaSynRM, similar performance was required of the two motors. The acceleration from 0-100 km/h in 10 s, which was one of the motor requirements, was used as the common performance level. After the parametric optimisation, the PMaSynRM had a time to 100 km/h of 8.83 s. This means that the motor size can be reduced and handle the performance requirements, while reducing the amount of material and weight of the motor.

4.5.1 Reduction of the stator yoke

The outer diameter of the motor was reduced by decreasing the size of the stator yoke. This has an effect on the time-varying magnetic field passing through the stator. The area of the stator yoke determines the flux density in the stator yoke. If the density is too high, it will saturate the stator yoke and affect the performance of the motor. Different outer diameters were simulated and are presented in Table 4.8. It was found that the diameter could be reduced by 15 mm, resulting in a reduction of the time to 100 km/h by 1.12 % , while reducing the total volume and weight of the motor by 14 % and 16 % respectively.

Table 4.8: Simulated reduced outer diameter of the stator.

Diameter (mm)	Volume (cm^3)	Weight (kg)	Time to 100 km/h (s)
240	6,111.5	42.7	8.80
-5	-285.7	-2.2	8.81
-10	-577.3	-4.5	8.83
-15	**-874.7**	**-6.9**	**8.90**
-20	-1,178.1	-9.3	9.09
-25	-1,487.3	-11.7	9.52
-30	-1,802.5	-14.2	10.46

4.5.2 Reduction of the motor length

Reducing the length of the motor decreases the maximum output torque. With a reduced outer stator diameter of 15 mm, the motor was simulated with different lengths, starting with the initial length of 150 mm and reducing it while ensuring that the performance requirements were met. Table 4.9 presents the results, where the motor could be decreased by 25 mm while keeping the same time to 100 km/h. The motor could be reduced by an additional 25 mm, down to a motor length of 100 mm, and still achieve a time to 100 km/h in under 10 s. Thereby reducing the volume and weight of the motor by 33 % and 34 % respectively.

Table 4.9 show that the time to 100 km/h was improved for a length reduction of up to 20 mm. Reducing the length of the motor to 140 mm decreases the maximum torque but also increases the base speed, see Fig. 4.7a. It results in a motor with

Table 4.9: Simulated reduced motor length.

Length (mm)	Volume (cm^3)	Weight (kg)	Time to 100 km/h (s)
150	5,236.8	35.8	8.90
140	-349.1	-2.4	8.85
130	-698.2	-4.9	8.86
125	-872.8	-6.1	8.91
120	-1,047.4	-7.3	8.98
110	-1,396.5	-9.8	9.24
100	**-1,745.6**	**-12.2**	**9.72**
95	-1,920.1	-13.4	10.07

lower maximum torque up to 55 km/h, but a higher torque at higher speeds, resulting in a lower time to 100 km/h, see Fig. 4.7b. The figures also show the performance of the 125 mm motor, which has a similar time to 100 km/h as the 150 mm motor despite a different torque characteristic.

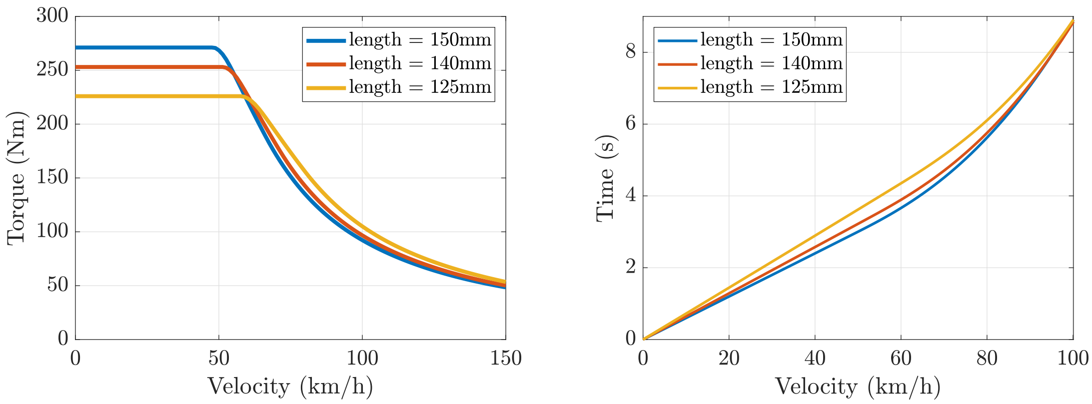

(a) Torque and base speed difference between motor lengths.

(b) Time difference between motor lengths.

Figure 4.7: Performance comparison between different motor lengths.

Fig. 4.8 shows a performance comparison of the motor before and after the size adjustments. It is clear that a reduction of the outer stator diameter by 15 mm, resulted in a small decrease of the maximum output torque and a negligible change to the time to 100 km/h. Fig. 4.8b shows that despite the different torque characteristic, as seen in Fig. 4.8a, the 100 mm motor has similar acceleration time to 110 km/h and a faster time to the required maximum speed of 150 km/h.

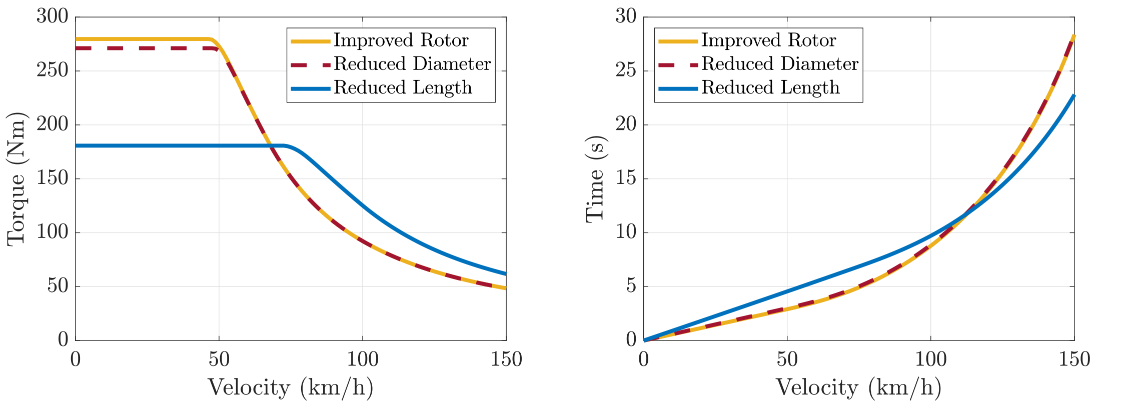

(a) Torque and base speed difference before and after the size adjustments.

(b) Time difference before and after the size adjustments.

Figure 4.8: Performance before and after the size adjustments.

4.6 Final design of the PMaSynRM

The parametric optimisation and the size adjustments resulted in the final design of the PMaSynRM, depicted in Fig. 4.9. The key performance factors and parameters of the motor are described in Table 4.10.

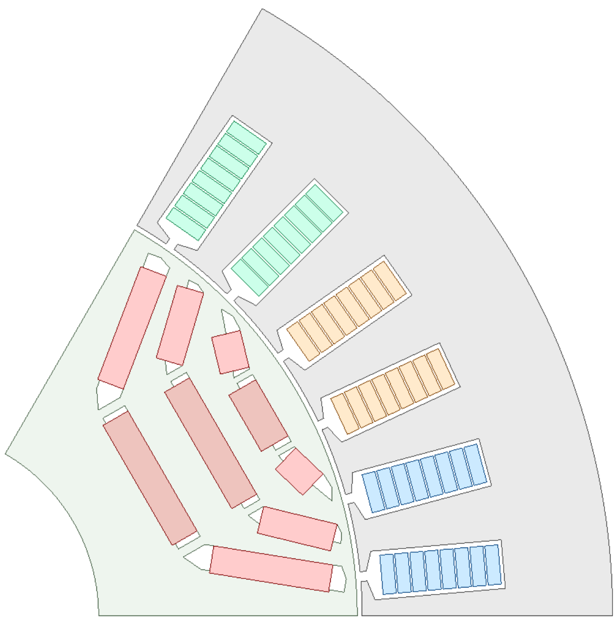

Figure 4.9: Final design of the PMaSynRM.

Table 4.10: PMaSynRM parameters.

Peak power	110 kW
Maximum torque	180 Nm
Time to 100 km/h	9.72 s
Base speed	5,800 rpm
Maximum speed	12,000 rpm
Gear ratio	7.78
DC Voltage	400 V
Maximum current (rms)	350 A
DC resistance	9.8 mΩ
Slot fill factor	65 %
Number of poles	6
Number of slots	36
Stator outer diameter	225 mm
Rotor outer diameter	143 mm
Stack length	100 mm
Air gap width	0.8 mm

5

FEM Analysis of the Motor

This chapter presents the simulation setup in Ansys Electronics as well as studies conducted to investigate the eddy current effects in hairpin winding and the potential risk of demagnetisation in the ferrite magnets.

5.1 Simulation setup

This section describes the analysis setup in Ansys Electronics. The definition of the currents are described as well as the settings for the solver and the mesh operation.

5.1.1 Current excitation

Since the hairpin conductors are defined as solid, the number of parallel paths have to be set to 1 in the winding excitation. To account for the decreased current in each conductor due to the addition of parallel branches, the current magnitude has to be divided by the number of parallel branches $N_{parallel}$. Further, in the post-processing of the data from Ansys, the Flux Linkage and the Induced Phase Voltage has to be scaled by $1/N_{parallel}$, while the Phase Current is scaled by $N_{parallel}$. In the simulation setup the three-phase current excitation of the windings were therefore defined as

$$i_a = \frac{\sqrt{2}}{N_{parallel}} i_s \cos(\omega t + \beta) \tag{5.1}$$

$$i_b = \frac{\sqrt{2}}{N_{parallel}} i_s \cos(\omega t + \beta - \frac{2\pi}{3}) \tag{5.2}$$

$$i_c = \frac{\sqrt{2}}{N_{parallel}} i_s \cos(\omega t + \beta + \frac{2\pi}{3}) \tag{5.3}$$

where $N_{parallel} = 2$ and the stator current i_s was defined using the relation between d- and q-axis current according to (2.24). The current angle β was defined as

$$\beta = tan^{-1} \left(\frac{i_q}{i_d} \right) \tag{5.4}$$

For the MTPA analysis, described further in Section 6.1, a parametric sweep of i_d and i_q is defined with a linear step of 50 A from −500 to 0 A and from 0 to 500 A for i_d and i_q respectively.

5.1.2 Analysis setup and resolution

The solver setup in Ansys was done for both lower and higher resolution simulations. Simulations with lower resolution were done during the design phase and parametric optimisation of the motor. The lower resolution shortens the simulation time significantly and was used due to the large amount of simulations in the design phase. Higher resolution simulations were conducted for the eddy current loss analysis further described in Section 5.2, and for the final analysis done with the MTPA controller and powertrain model as will be described in Chapter 6. The solver is a transient setup with a stop time defined as

$$t_{stop} = N_{periods} t_{step} N_{steps} \tag{5.5}$$

where $N_{periods}$ is the number of electrical periods, N_{steps} is the number of time steps per electrical period and t_{step} is the step time defined as

$$t_{step} = \frac{60}{\Omega_{rpm}\, p} \frac{1}{N_{steps}} \tag{5.6}$$

where Ω_{rpm} is the mechanical rotational speed of the motor and $60/(\Omega_{rpm}\, p)$ is the time of one electrical period in seconds. For the low resolution simulations, $N_{steps} = 120$ and $N_{periods} = 1$. While for the high resolution simulations, $N_{steps} = 180$ and $N_{periods} = 2$. Two electrical periods are necessary for the high resolution simulations since the hysteresis losses require one electrical period to stabilise.

5.1.3 Mesh settings

The mesh settings of the PMaSynRM are divided into different parts of the model. In general, a length based mesh inside the selected object was used with an unrestricted maximum number of elements. The rotor was split into two parts since it is required to have a good mesh density in the area of the rotor close to the air gap. This is due to the high saturation around the permanent magnets by the tangential ribs. Similarly, the stator was split into three parts consisting of the stator yoke, teeth and the area closest to the air gap. Further, the mesh settings had both low and high resolution with the higher resolution having a finer mesh. The maximum element length for low and high resolution is presented in Table 5.1. The hairpin winding and the magnets had a finer mesh for the high resolution simulations to account for the eddy current effects within the objects. The high resolution mesh for the PMaSynRM is depicted in Fig. 5.1a.

Table 5.1: Mesh settings for the low and high resolution simulations of the PMaSynRM as well as the settings for the round-wire winding and the area around the magnets for the reference motor only.

Property	Max length (mm) Low resolution	High resolution
Hairpin conductor	2	1
Round-wire winding	-	2
Magnets	3	2
Rotor	4	4
Rotor fine	2	1
Stator	4	4
Stator teeth	4	3
Stator teeth fine	4	2
Area around magnets	-	1

The mesh settings for the reference motor was done in a similar manner to the PMaSynRM. However, only high resolution simulations were conducted. Further, the conductors had a slightly larger maximum length since the eddy effects in the round-wire winding are negligible. Moreover, the rotor area around the magnets had a finer mesh setting. The settings are presented in Table 5.1 and the mesh can be seen in Fig. 5.1b.

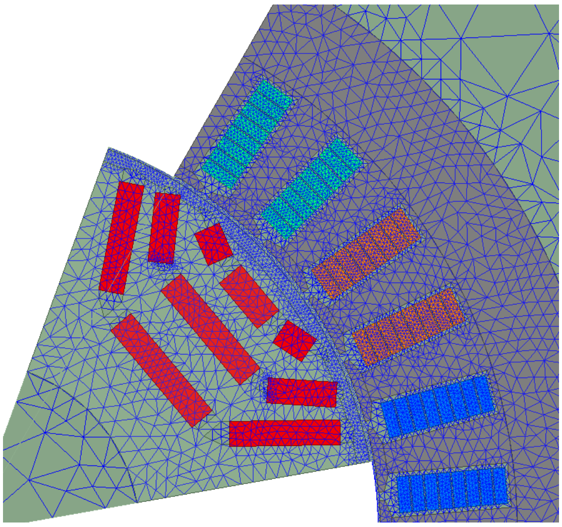

(a) PMaSynRM.

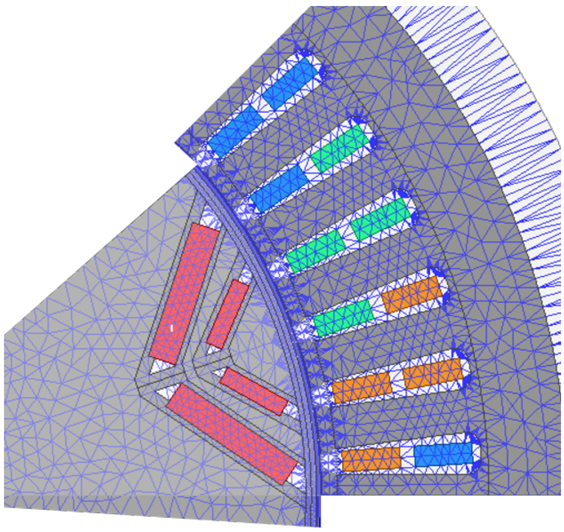

(b) Reference motor.

Figure 5.1: Mesh plots of the PMaSynRM and reference motor.

5.2 Eddy current loss analysis in hairpin winding

The influence of eddy current effects on the winding losses has been investigated in order to find an analytical method of estimating the frequency dependent losses. This was done to obtain reasonable losses at higher speeds for the final analysis with the MTPA controller and Simulink model, as will be described in Chapter 6. In order to obtain the frequency dependent winding losses, the simulation was setup with a sweep of the speed of the motor between 500 and 12,000 rpm with steps of 500 rpm. This corresponds to the operating range of the intended motor in this report. As described in Section 5.1.2, the step size and simulation stop time is dependent on the speed of the motor. In this way, the rotor rotates the same amount for each increment of the speed. The speed sweep was implemented in Python due to limitations observed with the Optimetrics function in Ansys Electronics, since changing the speed affects the simulation time step size. The simulation was therefore restarted for each increment of the speed. Further, to achieve a good resolution of the influence of eddy effects and the time-varying magnetic field on the conductors, a fine mesh with a maximum length varying between 0.1, 0.5 and 1 mm was studied. It was found that a mesh of 1 mm inside the conductors yielded the same results as 0.1 mm and was therefore chosen. Finally, the operating point of the motor was initially chosen as the combination of i_d and i_q found at base speed and at maximum allowed rms current magnitude. At this point, found through the procedure described further in Section 6.1, the currents $i_d = -425/\sqrt{2}$ and $i_q = 252/\sqrt{2}$. The losses were later on investigated with a decreased currents to observe the influence of the operating point.

The three-phase winding losses were obtained for different speeds from the Solid Loss quantity in Ansys. For this analysis, the end winding has been neglected as the eddy effects are considerably lower and for easier estimation of the phase resistance. The simulated losses were compared to an analytical loss model calculated with the average resistance factor of the conductors in a slot (2.41) as described in Section 2.4.3.1. The ratio of AC and DC winding losses is presented in Fig. 5.2a, where it can be seen that the simulated losses increase more with the frequency than the analytical model.

For a better understanding of the winding losses, the loss distribution was examined for the conductors in one slot. The losses in each individual conductor was obtained with the Field Calculator function in Ansys which was setup to calculate the Ohmic Losses for a given surface integral. In the post-processing of the data obtained from the Field Calculator, a factor corresponding to the length of the motor times the number of slots per phase and the number of pole pairs was multiplied to the losses to get the correct values. This was then compared to the analytical model (2.38), described in Section 2.4.3.1, which calculates the resistance factor for the kth winding layer of conductors in a slot. The resulting simulated and analytical loss ratio can be seen in Fig. 5.2b. The conductors with higher losses corresponds to the conductors closer to the slot opening.

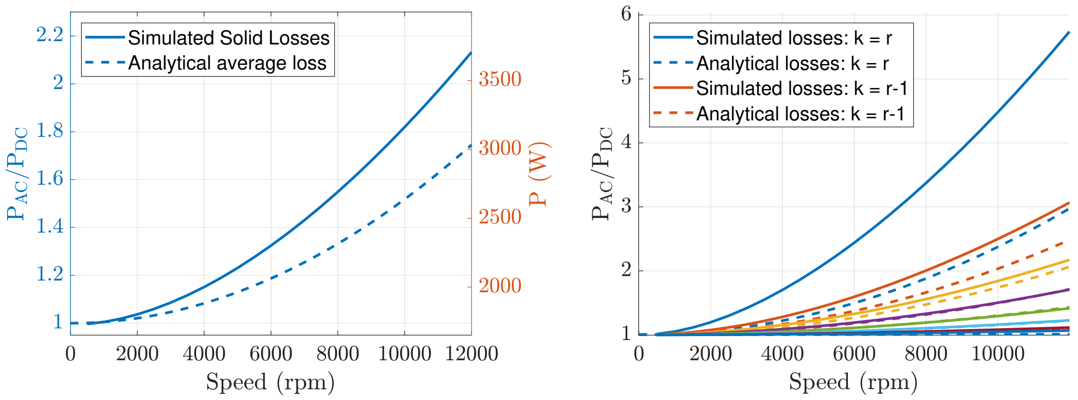

(a) Total winding losses and average analytical loss model.

(b) Winding losses for the kth conductor in a slot, where $k = r$ is the conductor closest to the slot opening.

Figure 5.2: The simulated ratio of AC and DC winding losses as a function of the speed compared to analytical models.

When comparing the simulated and analytically calculated losses, as seen in Fig. 5.2, it is clear that the simulated winding losses increase more with the frequency than what the analytical model accounts for. One study investigating the eddy current losses in hairpin winding found similar results and states that the AC losses are heavily affected by the time-varying leakage flux across the slot [29]. The leakage flux is strongest closest to the slot opening which significantly affects the nearby conductors, resulting in a large increase of the resistance at higher speeds. This phenomena can be seen in Fig. 5.2b where it is clear that the loss distribution is very uneven. It can also be observed that the analytical model is better matched to the simulated losses for conductors further away from the slot opening where the influence of the leakage flux is lower.

The influence of the operating point was also studied. The stator current magnitude influences the magnitude of the time-varying magnetic field that crosses the stator slots, causing the uneven current distribution. The values for i_d and i_q used in the previous simulations were decreased by 50 % and the resulting P_{AC}/P_{DC} ratio for the total winding losses as a function of speed can be seen in Fig. 5.3a. The figure also presents the average analytical loss model calculated with the decreased current magnitude. Further, the losses of each individual conductor in the slot is shown in Fig. 5.3b together with the analytical loss model for the kth layer. It is clear that the difference between the analytical model and the simulated losses is significantly reduced with the decreased current magnitude, compared to the results in Fig. 5.2. It can also be seen that the losses of the conductor closest to the air gap is affected the most by the operating point. Additionally, the loss distribution of the conductors in the slot correlates more to the analytical model. It is mainly the conductor closest to the air gap that has a higher frequency dependent loss dependency.

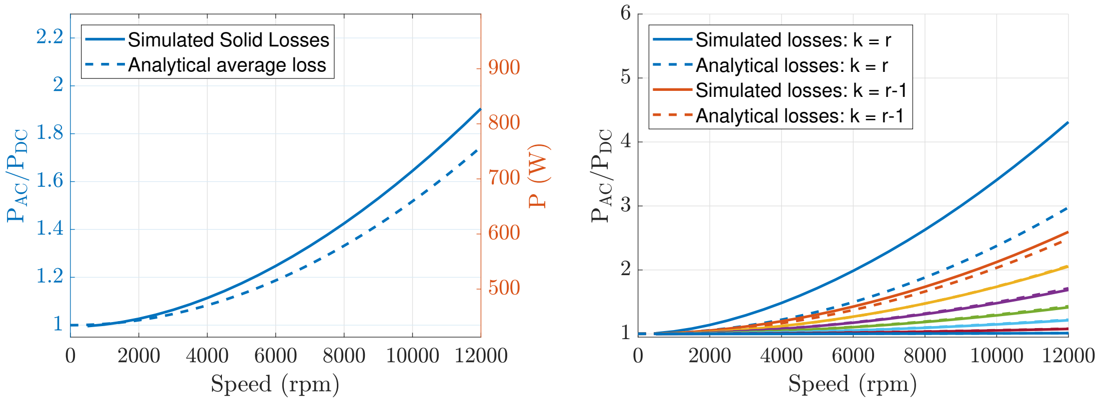

(a) Total winding losses and average analytical loss model.

(b) Winding losses for the kth conductor in a slot, where $k = r$ is the conductor closest to the slot opening.

Figure 5.3: The simulated ratio of AC and DC winding losses as a function of the speed compared to analytical models, with half the maximum current magnitude.

An empirical model was created by introducing a correction factor to the average analytical resistance factor. This was done to better capture the increased winding losses due to the time-varying leakage flux that is dependent on the operating point. The empirical model is defined as

$$k_R = \varphi(\xi) + 1.5\left(\frac{r^2 - 1}{3}\psi(\xi)\right) \tag{5.7}$$

and was used together with the analytical model for further analysis of the motor losses. A comparison of the two models and the simulated AC/DC winding loss ratio can be seen in Fig. 5.4.

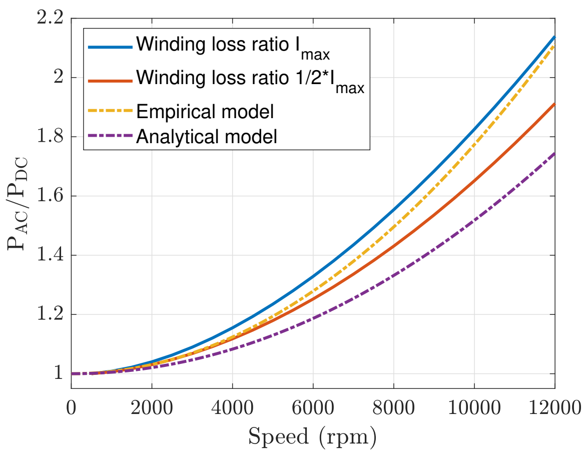

Figure 5.4: Empirical model compared to the analytical model and simulated AC/DC winding loss ratio at different current magnitudes.

5.2.1 Analysis of the conductor material on winding losses

The influence of conductor material on winding losses has been studied to compare aluminium winding to copper. Aluminium has a lower conductivity than copper which leads to a higher DC loss component. However the lower conductivity also leads to a decreased influence of the eddy current effects at higher frequencies. The AC/DC winding loss ratio as a function of speed was investigated for the same simulation setup but with the winding material replaced with copper. An analytical model of the average resistance factor was also calculated with the material definition of copper as specified in Appendix A.1. The results of the simulated and analytical winding loss ratios with copper winding is presented in Fig. 5.5 compared to the results from the study with aluminium winding. From the figure it can be seen that the DC loss component of copper is about 34 % lower than for aluminium. However, at higher speeds the winding losses of copper surpasses the winding losses of aluminium. This is seen for both the simulated and the analytically calculated losses. Depending on the operating region of the motor, the winding losses could potentially be similar for aluminium and copper hairpin winding.

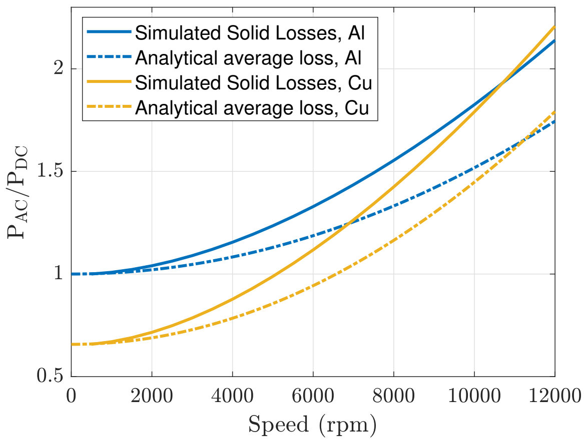

Figure 5.5: Comparison of the simulated and analytical winding losses for aluminium and copper conductors.

5.3 Demagnetisation study

As was discussed in Section 2.5, demagnetisation of the magnets can occur when an external magnetic field is counteracting the internal magnetic field of the magnets. To evaluate the safe operating region of the motor, the risk of demagnetisation was investigated. Ferrite magnets are sensitive to temperature and the critical flux density is higher for lower temperatures. At an operating temperature of -20 °C, the critical flux density for the FB9B magnets is between 0.13-0.16 T. Further, the external magnetic field that counteracts the internal magnetic field of the magnets is related to the magnitude of the negative current i_d. It was found that by increasing i_q and keeping i_d constant, the risk of demagnetisation was reduced. The study was therefore conducted by decreasing i_d from 0 A down to the maximum allowed current, while i_q was set to 0 A. The flux density in the magnets was observed to evaluate at which magnitude of i_d the critical flux density was reached. In Fig. 5.6a it can clearly be seen that large parts of the magnets are demagnetised when $i_d = -I_{max}^{rms}$. For a lower current of $i_d = -200$ A rms, the magnetic flux density is above the critical flux density of the magnets as can be observed in Fig. 5.6b. For safe operation of the motor, the magnitude of i_d must be kept below 200 A to ensure that the magnets stay magnetised.

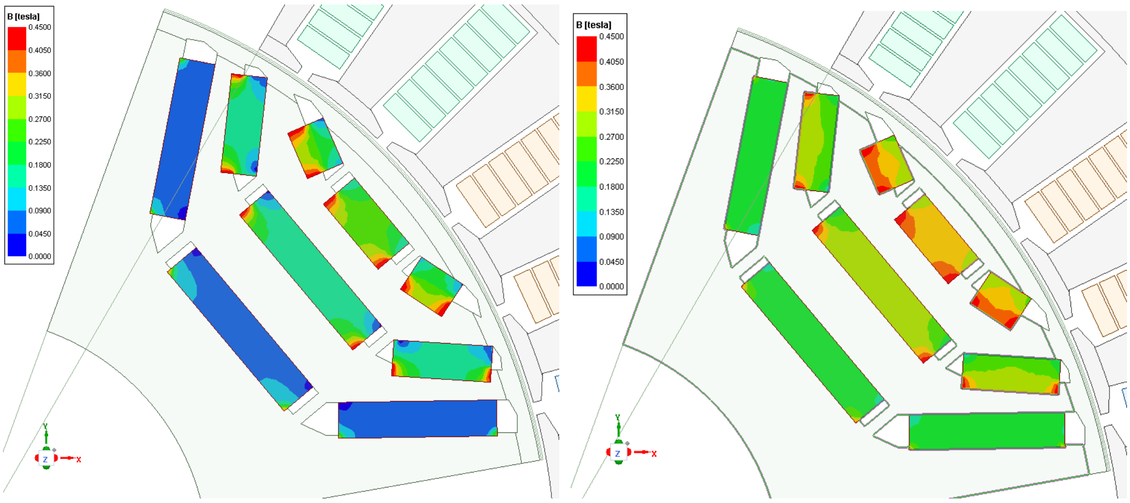

(a) Flux density in the magnets at $i_d = -350$ A rms.

(b) Flux density in the magnets at $i_d = -200$ A rms.

Figure 5.6: Demagnetisation of the magnets.

6

MTPA Controller and Powertrain Model

6.1 MTPA

A field-oriented control strategy, MTPA, has been used to control the operation of the motor. The underlying theory of MTPA has been described in Section 2.3. The aim of this control strategy is to map the operating region of the motor, while minimising the resistive losses by minimising the current magnitude for a certain torque. The MTPA controller was implemented in Matlab and was used in the post processing of the data obtained from Ansys Electronics. The data exported from Ansys is a transient data table containing different quantities, defined in Table 6.1. The quantities are functions of different combinations of i_d and i_q.

Table 6.1: Imported quantities from Ansys Electronics for post process analysis.

Description	Variable	Unit
Time	t	(s)
3-phase Flux linkage	Ψ_{abc}	(Wb)
3-phase Induced voltage	V_{abc}	(V)
3-phase Input current	i_{abc}	(A)
Torque	T	(Nm)
Core loss	P_{core}	(W)
Eddy current loss	P_{eddy}	(W)
Hysteresis loss	P_{hyst}	(W)
Solid loss	P_{solid}	(W)
Stranded loss	$P_{stranded}$	(W)
Moving position	θ	(rad)

The maximum torque per ampere is obtained with the $fmincon$ function in Matlab, which finds the minimum of a constrained nonlinear multivariable function. Further, the MTPA Matlab code makes a sweep of the speed in rpm and maps all the quantities through interpolation. The resolution of this analysis is based on the step size of the speed as well as the torque. For this report, $n_{step} = 100$ rpm and $T_{step} = 10$ Nm. The maximum torque as a function of speed was obtained for both the reference motor and the PMaSynRM. This is shown in Fig. 6.1 together with the output power curves of the two motors.

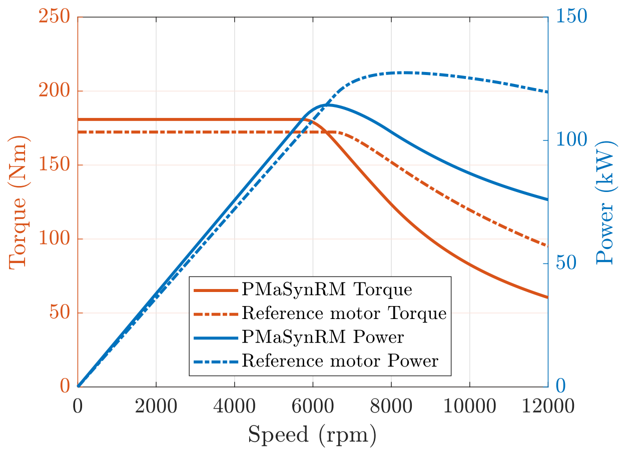

Figure 6.1: Maximum torque and output power for the PMaSynRM and the reference motor.

A plot of the MTPA operating points can be seen in Fig. 6.2, which shows the operating region of the motor in the dq-plane. The combinations of i_d and i_q that form the operating region in the dq-plane were calculated from the points of the operating region in the torque-speed plane limited by the maximum torque line, as shown in Fig. 6.1. The MTPA plot in Fig. 6.2 also depicts the voltage and current limits for a sweep of the electrical speed and stator current respectively. Further, the torque hyperbola is presented, which indicates the points of constant torque.

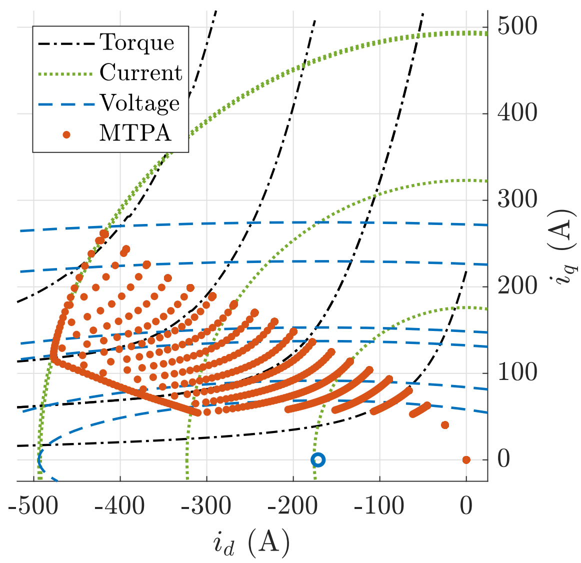

Figure 6.2: MTPA curve for the PMaSynRM.

6.1.1 Motor loss analysis

For the whole operating region, the motor losses were calculated. Regarding the winding losses, both an analytical and an empirical model of the resistance factor were investigated, as described in Section 5.2. The winding losses for the PMaSynRM with the analytical model can be seen in Fig. 6.3a, while Fig. 6.3b shows the winding losses for the empirical model where the increased losses can be observed. The introduction of the resistance factor also has an effect on the induced voltage of the motor and thereby the performance, however this effect has a negligible difference between the two models. Further analysis of the PMaSynRM was therefore done with the empirical model as the loss estimation was closer to the simulated losses as discussed in Section 5.2. As for the reference motor, the eddy current effects in the winding is not as prevalent due to the small size of the round-wire conductor. Due to this, the winding losses were calculated with the DC resistance.

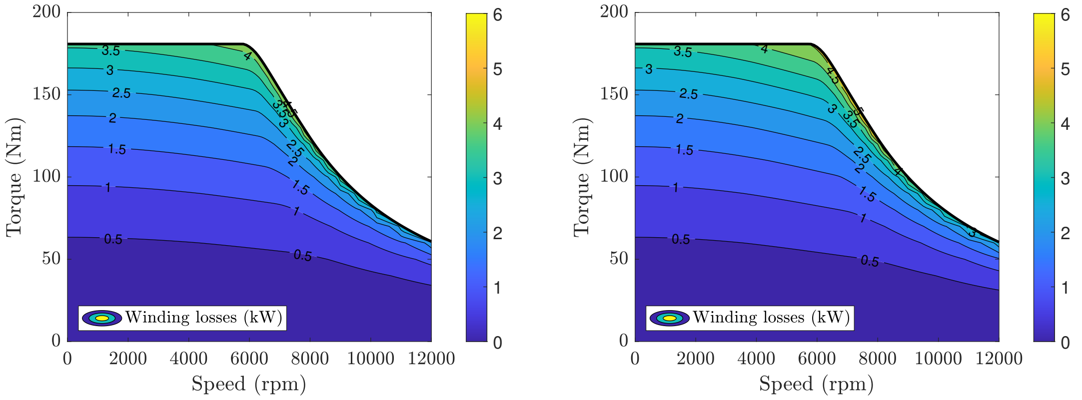

(a) Analytical model. **(b)** Empirical model.

Figure 6.3: Winding loss map for the PMaSynRM.

Similar to the winding losses, the eddy current and hysteresis losses are dependent on the frequency. The frequency relation was studied by varying the speed of the machine and by observing the hysteresis and eddy current losses. It was found that the eddy current and hysteresis losses have a frequency dependency similar to their definitions (2.32) - (2.33), where the eddy current losses have a frequency dependency to the power of two and the hysteresis losses are linearly dependent on the frequency. To shorten the simulation time, by not requiring a sweep of the speed, the eddy current and hysteresis losses were scaled with a frequency ratio of the current speed divided by the speed at which the mapping was done according to the definitions of both loss components. Further, the hysteresis losses were scaled with a factor of 1.7 to account for degradation of the core lamination. The total losses including winding, eddy current and hysteresis losses, can be seen in Fig. 6.4 for the PMaSynRM and the reference motor.

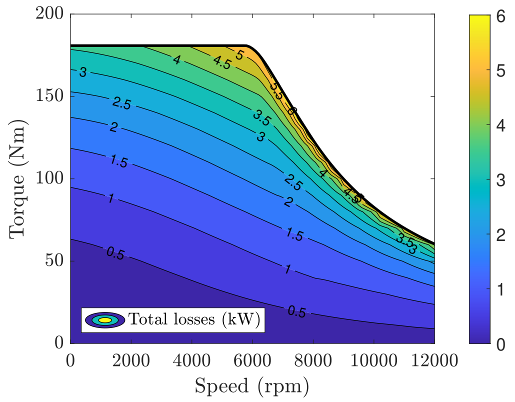

(a) PMaSynRM.

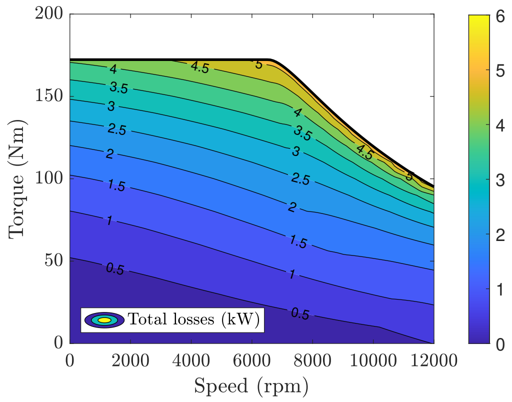

(b) Reference motor.

Figure 6.4: Total loss map for the PMaSynRM and the reference motor.

6.1.2 Impact of demagnetisation on the operating range

The operating region of the motor is limited due to the risk of demagnetisation as described in Section 5.3. The safe operating region, where the magnitude of i_d is below 200 A rms, was obtained from the addition of a constraint to the MTPA controller. The MTPA plot for the safe operating region can be seen in Fig. 6.5. Further, Fig. 6.6 shows the safe operating points in the torque-speed region, as well as the points were the risk of demagnetisation is high.

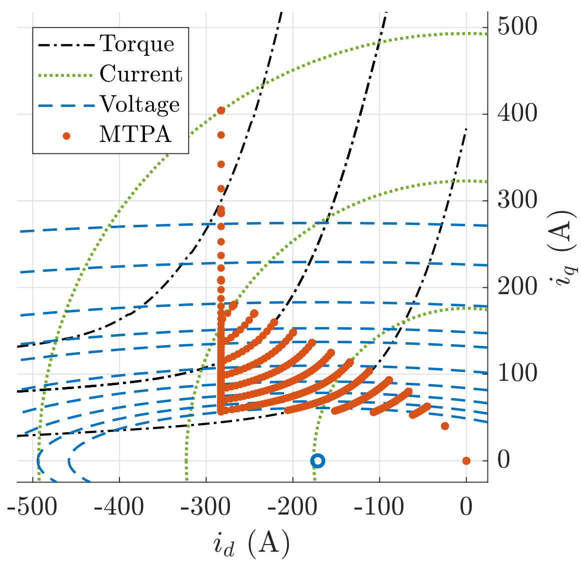

Figure 6.5: MTPA curve for the PMaSynRM with regards to demagnetisation.

To evaluate the performance of the motor, a model of the powertrain was designed as will be described in Section 6.2. In the evaluation of the PMaSynRM, the whole operating region of the motor was used and later compared to the limited performance for the safe operating region.

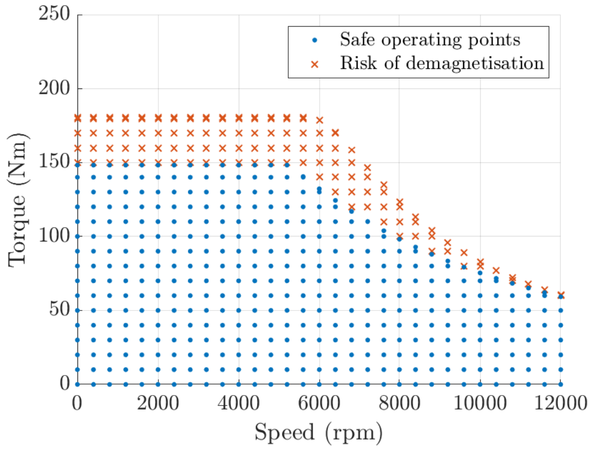

Figure 6.6: Approximate limited operating region of the motor due to risk of demagnetisation.

6.2 Model of the powertrain and physical model in Simulink

In this section, a simplified model of the powertrain constructed in Simulink is presented. The aim of the powertrain model is to test the performance and power requirements of the electric motor over different drive cycles. The model is depicted in Fig. 6.7 and includes a model of the vehicle dynamics, transmission and electric motor. The drive cycles have previously been discussed in Section 3.2 together with the intended vehicle model of this study. The drive cycle input provides a time series of velocities from the WLTP and CADC 150 drive cycles. The first subsystem, *Drive Cycle and Acceleration estimator*, uses that information to estimate the acceleration using the backwards Euler method. The next subsystem, *Vehicle Dynamics model & wheel torque calculation*, is based on the equations presented in Section 2.1 and calculates the angular velocity and required torque of the wheels from the speed and acceleration of the drive cycle. The *Transmission* subsystem adds the transmission losses to the required wheel torque, which according to [20] is assumed to be 5 %. The transmission also includes the gear ratio, which changes the torque and angular velocity.

As was discussed in Section 6.1, the MTPA controller provides the operating range of the motor with the current and voltage constraints described in Section 3.4. The MTPA controller also provides a map of the losses for the whole operating region of the motor. The required torque at a certain speed from the drive cycle gives the losses at each operating point of the drive cycle through interpolation. The final block, *Motor Losses*, adds the losses to the required power from the transmission during motor operation. In this study, it is assumed that regenerative braking is applied whenever the acceleration is below zero and that the motor losses are the same for regenerative and motor operation. Further, the maximum regenerated power is limited by the negative torque limiting line. During regenerative operation,

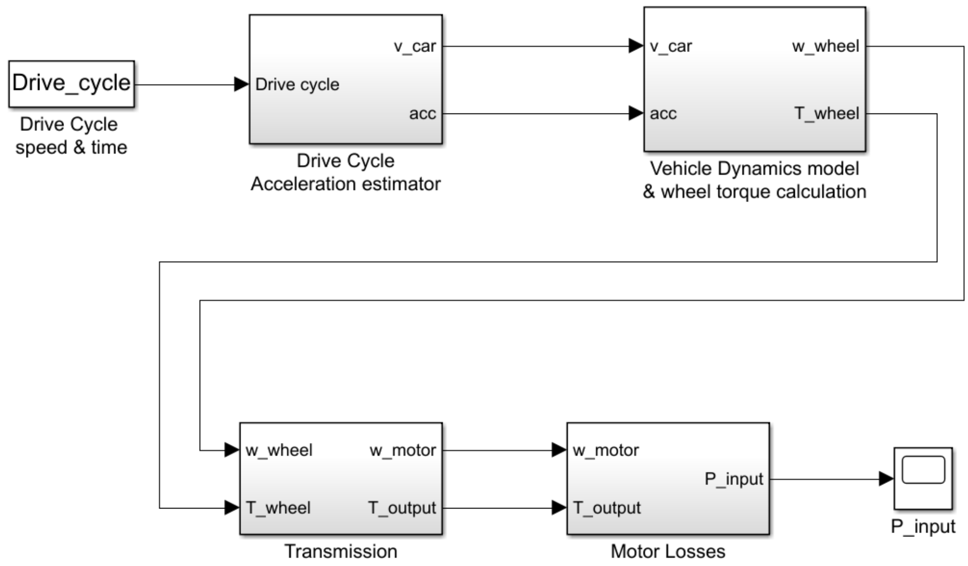

Figure 6.7: Overview of the simplified powertrain model in Simulink.

power is supplied from the wheels to the motor. In this case, the required power from the transmission is negative and the added motor losses reduces the power supplied to the motor, P_{input}. The total energy demand of the motor was obtained by integrating P_{input} and was used to determine the efficiency and energy consumption of the different motor designs based on reliable driving patterns.

6.2.1 Drive cycle performance comparison

The required torque operating points, T_{output}, from the WLTP and CADC 150 drive cycles can be seen in Fig. 6.8 together with the maximum torque lines of the PMaSynRM and the reference motor. As the figure shows, the required torque operating points, while accelerating, for both drive cycles are within the region limited by the maximum torque line of the PMaSynRM. As for the reference motor, one operating point is slightly outside of the limited region. However, this is negligible for this study since the reference motor has been scaled as a benchmark for a fair comparison to the PMaSynRM and has not been optimised. The majority of the required torque operating points, while decelerating, are also within the region for both motors. The points outside of the limiting torque lines have reached the maximum torque for regenerative breaking. The regenerated power is limited to the negative maximum torque at that speed, and beyond this point mechanical braking is applied.

6.2.1.1 Energy consumption and loss analysis of the WLTP drive cycle

The energy demand for the WLTP drive cycle can be seen in Fig. 6.9a together with the driving pattern of the drive cycle. E_{wheel} is the energy demand from the drive cycle based on the vehicle dynamics model. E_{output} is the required output energy from the motor, with the transmission losses taken into account. Finally, E_{input} is

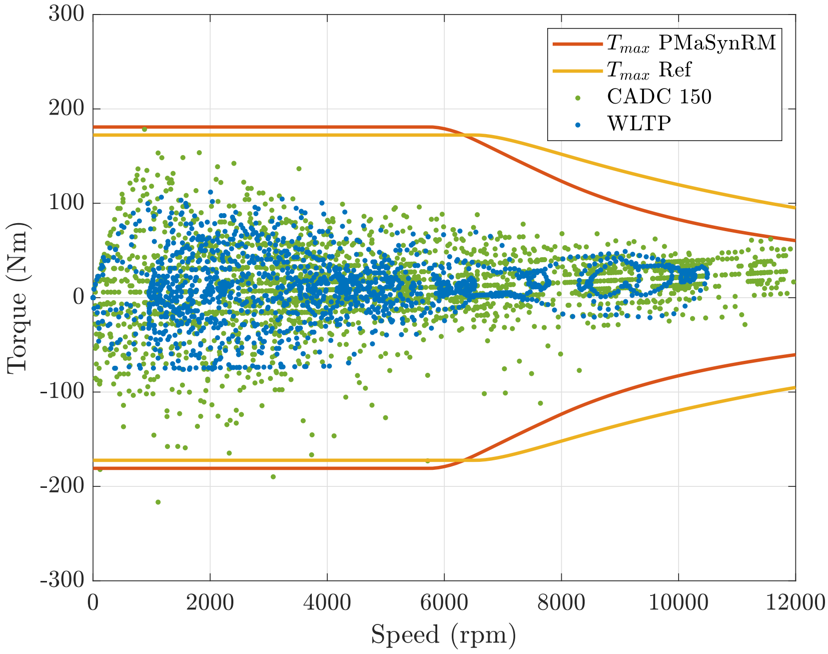

Figure 6.8: Torque demand of the drive cycles compared to the maximum torque lines of the two motors.

the energy supplied to the motor, with regards to the added losses of the motor. Fig. 6.9b shows the final part of the drive cycle, where it can be seen that the total energy demand of the PMaSynRM is slightly lower than the reference motor. For the PMaSynRM, 14.1 % of the energy was lost after completing the drive cycle compared to 15.0 % for the reference motor. Further, the energy consumption for the PMaSynRM is 16.1 kWh/100 km compared to 16.2 kWh/100 km for the reference motor.

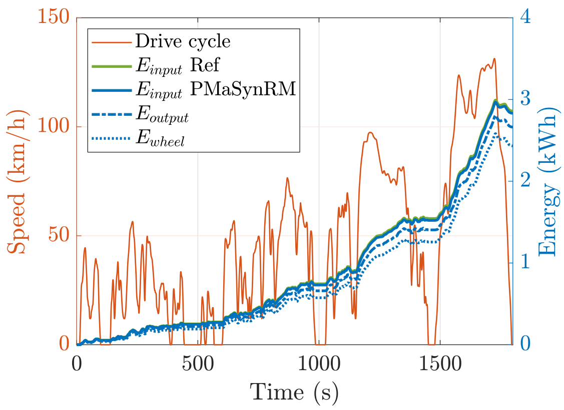

(a) Complete drive cycle.

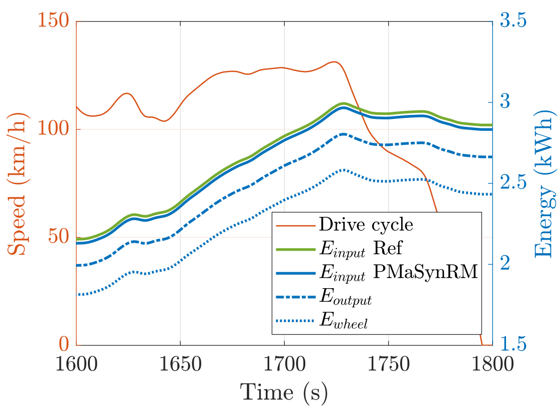

(b) Zoomed in.

Figure 6.9: Energy demand for the WLTP drive cycle comparing the two motors.

A comparison of the different motor losses for the PMaSynRM and the reference motor is shown in Fig. 6.10. Further, Fig. 6.10a shows that the winding losses for the aluminium hairpin conductors in the PMaSynRM is lower for low speed operation. The total winding losses, as seen in 6.10b, for the WLTP drive cycle is also lower despite the increased losses at higher speeds compared to the copper round-wire winding in the reference motor. Despite the higher winding losses for the PMaSynRM in the Extra High region, the combined losses are lower than for the reference motor. This is due to the higher hysteresis and eddy current losses caused by the larger flux density of the Nd(Dy)FeB magnets in the reference motor, as described by (2.32) - (2.33).

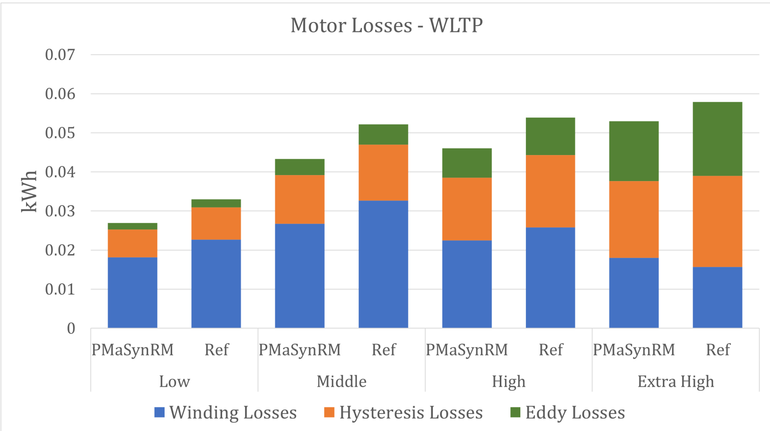

(a) Losses for different sections in the WLTP drive cycle.

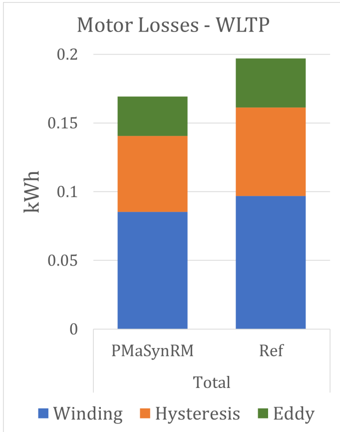

(b) Total losses for the WLTP drive cycle.

Figure 6.10: Loss analysis of the WLTP drive cycle for the two motors.

6.2.1.2 Energy consumption and loss analysis of the CADC 150 drive cycle

The energy demand for the CADC 150 drive cycle can be seen in Fig. 6.11 together with the driving pattern of the drive cycle. The total energy demand of the PMaSynRM is, similarly to the WLTP drive cycle, slightly lower than the reference motor. For the PMaSynRM, 13.3 % of the energy was lost after completing the drive cycle compared to 13.9 % for the reference motor. Further, the energy consumption for the studied vehicle model equipped with a PMaSynRM is 18.9 kWh/100 km compared to 19.0 kWh/100 km for the reference motor.

A comparison of the different motor losses for the PMaSynRM and the reference motor is shown in Fig. 6.12. Similarly to the WLTP drive cycle, the winding losses for the PMaSynRM is lower for low speed operation, as seen in Fig. 6.12a. The Urban and Road driving patterns corresponds to lower speed operation while Motorway represents high speed. The total winding losses, as seen in 6.10b, for the CADC 150 drive cycle is also lower despite the increased losses at higher speeds compared to the reference motor. The combined losses for the Motorway region are lower for the PMaSynRM, similar to the WLTP drive cycle. This is once again due to the higher hysteresis and eddy current losses of the reference motor.

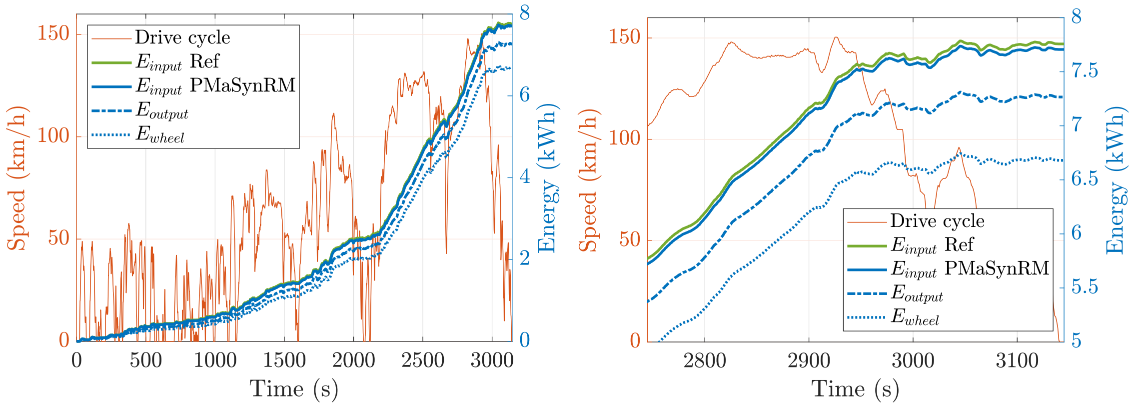

(a) Complete drive cycle. **(b)** Zoomed in.

Figure 6.11: Energy demand for the CADC 150 drive cycle comparing the two motors.

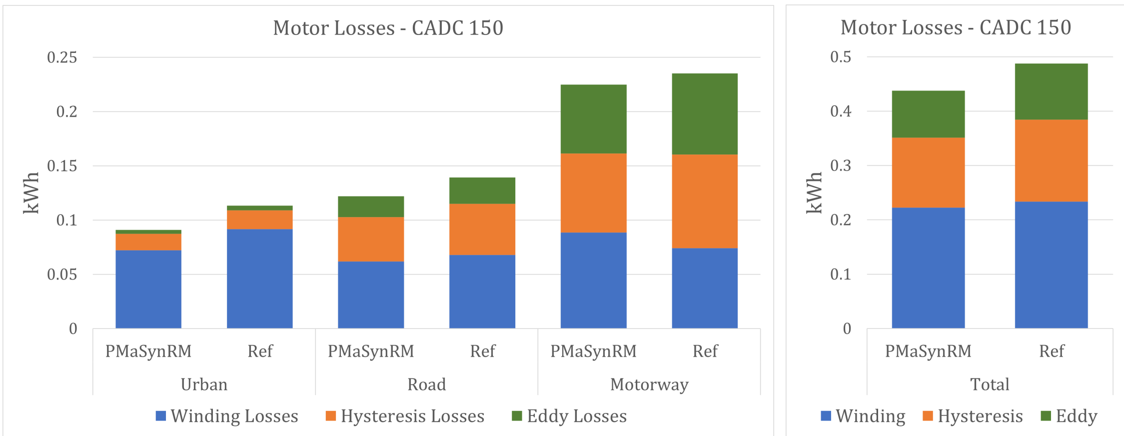

(a) Losses for different sections in the CADC 150 drive cycle. **(b)** Total losses for the CADC drive cycle.

Figure 6.12: Loss analysis of each section of the CADC 150 drive cycle for the two motors.

6.2.2 Limited performance due to demagnetisation

The maximum torque line is limited due to risk of demagnetisation, discussed in Section 6.1.2, and is given by the safe operating points. The required torque from the WLTP and CADC 150 drive cycles are shown in Fig. 6.13 together with the limited maximum torque line for safe operation. As can be seen, the performance of the PMaSynRM is heavily affected by the restricted operating points for safe operation. Despite this, the required torque operating points from the WLTP drive cycle are within the limited region for the PMaSynRM. Further, the motor can handle a majority of the torque operating points for the CADC 150 drive cycle, with limited acceleration in some regions. The time to 100 km/h for safe operation is 12.5 s.

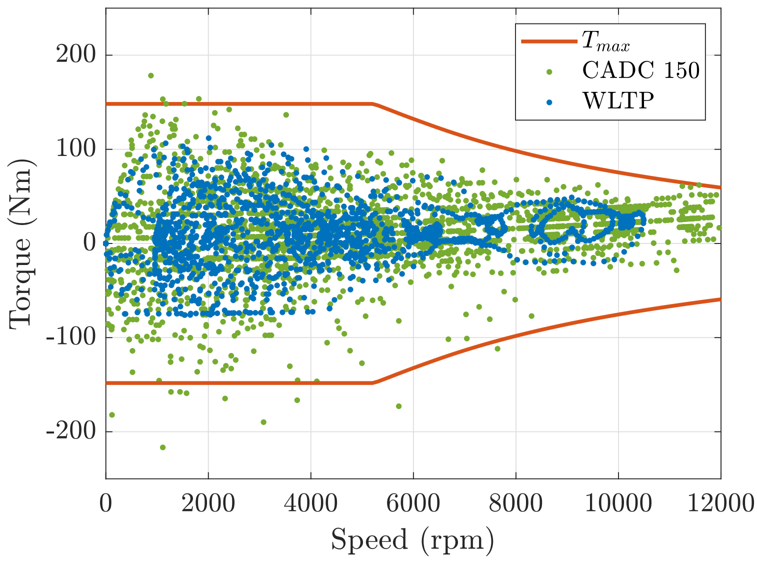

Figure 6.13: Limited maximum torque line of the PMaSynRM compared to the torque demand of the drive cycles.

7

Environment and Cost Analysis

This chapter presents the cost analysis of the different motors and the environmental impact in both ELU and carbon dioxide equivalence (CO_2-eq). The calculations are based on the raw material needed to produce the parts, including the scrap during production. Since some of the material goes to waste, the production of aluminium and copper require an extra 2 % of material [30], steel requires an additional 13.6 % [31], NdFeB magnets require 20 % and ferrite magnets require 27 % [32]. The cost and impact during production and recycling are not included.

7.1 Environmental Impact

There are many ways to measure how an element affects the environment. This thesis has used the two measurement systems Environmental Priority Strategies (EPS) and Global Warming Potential (GWP). Both systems were developed to simplify and enable faster comparisons between different materials.

7.1.1 Environmental Priority Strategies, EPS

The first version of the EPS system was developed in 1989, by cooperation between Volvo, IVL Swedish Environmental Research Institute and the Swedish Federation of Industries [33]. The purpose was to have a comparison between different products from a life cycle analysis (LCA) point of view [33][34]. The EPS system is based on the LCA standards ISO 14040 and ISO 14044. It aims to preserve the natural capital for the next generation in at least the same state as this generation inherited it from the previous generation [34]. A decrease in the capital needs to be replaced or compensated for. The compensation is expressed as a dept and measured in the economic value of ELU for each element. ELU expresses the environmental impact in euro/kg [9]. Rare materials generate a higher dept compared to commonly found materials.

Table 7.1 shows the ELU comparison of the different magnet and winding materials used in the PMaSynRM and the reference motor. From the table it is clear that aluminium winding and ferrite magnets have a substantially lower environmental impact. For the winding material, the reason is that aluminium is the third most common material in the earth's crust, while copper is more rare and therefore has a higher ELU value [9]. The density of aluminium is 70 % lower than the density of copper. However, a 38 % larger volume is needed for the aluminium hairpin conductors, due to the lower current density as explained in Section 4.3. Despite the increased volume, the weight of aluminium was 53 % lower than the weight of copper, as shown in Table 7.1.

Table 7.1: Environmental impact in ELU of the different magnet and winding materials used for the two motors.

		Volume (cm^3)	Density (g/cm^3)	Material amount (kg)	ELU (euro/kg)	Total impact (euro)	Difference in ELU (%)
Winding material	Copper	515.6	9.0	4.6	131.0	607.8	-
	Aluminium	813.7	2.7	2.2	0.2	0.35	-99.9%
Magnets	Nd(Dy)FeB	208.0	7.5	1.6	102.8	160.4	-
	FB9B	446.9	4.9	2.19	2.9	6.3	-96.1%

Both the change of magnet material and winding material greatly improves the ELU. However, a larger total volume of magnets is required when using ferrite compared to Nd(Dy)FeB magnets to handle the same requirements. It thereby increases the environmental impact but, as Table 7.1 shows, the difference in ELU between the magnets is so significant that the total impact of ferrite is still an immense improvement from an environmental point of view. Table 7.2 shows a more extensive comparison between the magnets, since they consist of several different elements. The table indicate which element has the largest environmental impact. The material amount of the Nd(Dy)FeB was obtained from a similar study by [5]. For the ferrite magnet, the material amount was calculated from the magnet composition presented by [35].

Table 7.2: Deeper comparison of the environmental impact of the magnet materials.

		Material amount (%)	ELU (euro/kg)	Total impact (euro/kg)	Total impact (%)
Nd(Dy)FeB	Neodymium	25.7	202.0	51.8	50%
	Dysprosium	3.3	1500.0	49.4	48%
	Iron	69.1	1.0	0.7	0.7%
	Boron	1.3	9.1	0.1	0.1%
	Nickel	0.7	124.0	0.8	0.8%
FB9B	Strontium	3.6	0.2	0.01	0.2%
	Lanthanum	0.8	175.0	1.4	48.1%
	Cobalt	0.3	205.0	0.7	23.5%
	Iron	80.9	1.0	0.8	28%
	Oxygen	14.4	0.0	0.0	0%

Table 7.3 sums the environmental impact of the two motors and compares the ferrite motor to the reference motor. As can be seen, the difference is immense. The ferrite

motor reduced the impact in ELU by 96.1 %. The biggest reduction does not come from the replacement of the rare-earth magnets but from using aluminium instead of copper. As the table shows, it reduces the impact by 99.9 %, from 607.8 euros to just 0.4 euros. The change from Nd(Dy)FeB to ferrite is also a great improvement, however, 77 % of the total impact of the reference motor is caused by the copper winding. This makes the change of winding material the most important to reduce the ELU.

Table 7.3: Environmental Impact in ELU of the two motors.

		Material amount (kg)	ELU (euro/kg)	Total Impact (euro)	Difference in ELU compared to corresponding part in reference motor (%)
Reference Motor	Nd(Dy)FeB magnet	1.56	102.8	160.4	-
	Copper winding	4.64	131.0	607.8	-
	Steel core	22.6	1.0	22.3	-
	Motor total	28.8	27.5	790.6	-
FB9B Motor	FB9B magnet	2.19	2.9	6.3	-96.1%
	Aluminium winding	2.20	0.2	0.4	-99.9%
	Steel core	24.4	1.0	24.2	+8.1%
	Motor total	28.8	1.1	30.8	-96.1%

7.1.2 Global Warming Potential, GWP

GWP is a another measurement of environmental impact which also strives to enable a faster comparison between different materials. However, GWP compares gases' impact on global warming [36]. It is a measurement of how much energy the emissions of 1 ton of gas will absorb compared to CO_2 during a specified period of time, usually 100 years is used. GWP is measured in the unit CO_2-eq and CO_2 thereby has the value of 1 CO_2-eq independent on the time frame. A larger value means that the gas warms the earth more than CO_2 would do during the same period of time. By translating the emissions of the gases to a common unit it is possible to add the emissions from several gases together.

In a study by [37], three motors were compared. One of them was a Nd(Dy)FeB magnet motor and one was a ferrite magnet motor, both with copper round-wire stator windings. The study investigated the total emissions during magnet production, motor production and when the motor was used. All three motors could accelerate from 0-50 km/h in around 3.2 seconds and were assumed to have a lifetime of 200 000 km. The study showed that the total impact in CO_2-eq was reduced by 13.12 % for the ferrite motor. Since the study by [37] only used copper winding, the difference in CO_2-eq for the raw material needed for the winding and core production of the two motors in this thesis is presented in Table 7.4 [38]. It shows a significant improvement when changing the winding material from copper to aluminium.

Table 7.4: GWP comparison of the motor material impact with different winding material.

		GWP 100 years (kg CO_2-eq/kg)	Motor material impact (kg CO_2-eq)	Motor material impact (g CO_2-eq/km)	Impact difference (%)
Nd(Dy)FeB Motor	Copper winding	8.3	38.5	0.2	-
	Steel core*	1.5	32.8	0.2	-
	Total	9.8	71.3	0.4	-
FB9B Motor	Aluminium winding	8.2	18.0	0.1	-53%
	Steel core*	1.5	35.4	0.2	+8%
	Total	9.7	53.4	0.3	-25%

*The steel core consists of iron with up to 3.2 % silicon but [38] only presents the data for iron, so GWP for silicon is not taken into account [39].

7.2 Cost Analysis

Using different materials not only affects the environmental impact but also impacts the cost of the motors. Therefore, a cost analysis was performed and was based on the cost of the required raw materials. Table 7.5 compares the magnets and presents how much each element in the respective magnet contribute to the total cost of it. Iron is the main material in both magnets and for the ferrite magnet, it is the main cost contributor. However, for the Nd(Dy)FeB magnet, the neodymium is responsible for 71 % of the total cost.

Table 7.5: Deeper comparison of the environmental impact for magnet materials.

		Material amount (%)	Cost (USD/kg)	Total cost (USD/kg magnet)	Total cost (%)	Price reference
Nd(Dy)FeB	Neodymium	25.7	209.0	53.6	71 %	[40]
	Dysprosium	3.3	601.3	19.8	26 %	[40]
	Iron	69.1	3.0	2.1	3 %	[41]
	Boron	1.3	9.4	0.1	0 %	[42]
	Nickel	0.7	32.1	0.2	0 %	[11]
FB9B	Strontium	3.6	1.0	0.03	1 %	[43]
	Lanthanum	0.8	4.4	0.03	1 %	[40]
	Cobalt	0.3	82.0	0.3	10 %	[11]
	Iron	80.9	3.0	2.4	88 %	[41]
	Oxygen	14.4	0.0	0.0	0 %	-

Table 7.6 presents a comparison of the two motors which indicates that the ferrite magnets are substantially cheaper. The winding material also has a big influence on the total cost. It is clear that the motor cost can be heavily reduced by both changing to aluminium winding and ferrite magnets.

Table 7.6: Cost comparison of the two motors.

		Material amount (kg)	Cost (USD/kg)	Total cost (USD)	Reduced cost compared to corresponding part in reference motor (%)	Price reference
Reference Motor	Nd(Dy)FeB magnet	1.6	76.0	118.5	-	Table 7.5
	Copper winding	4.6	10.3	47.8	-	[11]
	Iron core	22.6	1.3	28.9	-	[40]
	Motor total	28.8	6.8	195.2	-	-
FB9B Motor	FB9B magnet	2.2	2.8	6.1	-94.9 %	Table 7.5
	Aluminium winding	2.2	3.5	7.7	-84.0 %	[11]
	Iron core	24.4	1.3	31.2	8.1 %	[40]
	Motor total	28.8	1.6	45.0	-77.0 %	-

8 Conclusion

In this thesis, a PMaSynRM with ferrite magnets and aluminium hairpin winding was designed and compared to a reference PMSM with Nd(Dy)FeB magnets and copper round-wire winding. For the requirements stated in this study, the PMaSynRM had a similar performance to the reference motor. The two motors had an acceleration from 0-100 km/h in 9.72 s and 9.82 s respectively and could handle both the WLTP and CADC 150 drive cycles. Despite the frequency dependent losses of hairpin winding, due to eddy current effects, the aluminium hairpin winding had lower total winding losses than the copper round-wire for both drive cycles. Further, the lower flux density of the ferrite magnets resulted in lower hysteresis and eddy current losses compared to the Nd(Dy)FeB magnets in the reference motor. However, the ferrite magnets are at risk of demagnetisation for large current magnitudes. This results in a limited operating region for safe operation of the PMaSynRM. Despite this, the PMaSynRM could still complete the WLTP drive cycle and a majority of the CADC 150 drive cycle.

An environmental and cost analysis was conducted for the two motors to investigate the impact of the different materials. The environmental impact was measured with the EPS system, which aims to preserve the natural capital, and is measured in the economic value of ELU. It was found that the PMaSynRM had a 96.1 % lower total impact in ELU compared to the reference motor. The impact of the ferrite magnets was 96.1 % lower than the Nd(Dy)FeB magnets, while aluminium was 99.9 % lower than copper regarding the winding. Further, the aluminium hairpin winding had a 53 % lower CO_2-eq compared to the copper round-wire. The total cost of the PMaSynRM was found to be 77.0 % lower than the PMaSynRM. The ferrite magnets had a 94.9 % lower cost than the Nd(Dy)FeB magnets, while the cost for the aluminium hairpin winding was 84.0 % lower compared to the copper winding in the reference motor.

8.1 Future work

The results presented in this thesis regarding the performance of the PMaSynRM and the reference motor are based on the requirements and assumptions made throughout the study. The requirements set for the motors were quite low compared to the performance of many existing electric motors in the market. Perhaps the results for the performance comparison would differ more if the motors were optimised with regards to tougher requirements.

Further improvements to the rotor structure could be necessary, and a more extensive optimisation of the rotor variables could be done with a more advanced algorithm, using an optimisation software. Moreover, an investigation of the mechanical stresses in the rotor is necessary to validate the design. Further, the mechanical limitations on the rotor structure could be included in the optimisation of the rotor variables. A thermal analysis can also be done to investigate the impact on the ferrite magnets and the winding losses of the aluminium hairpin conductors. Additionally, the limited performance of the safe operating region with regards to the risk of demagnetisation could be improved by investigating different ferrite magnets. Another possible solution could be to use a combination of ferrite and NdFeB magnets.

Bibliography

[1] *How much air pollution comes from cars?* [Online]. Available: `https://auto.howstuffworks.com/air-pollution-from-cars.htm` (visited on 03/08/2022).

[2] *Volvo cars to be fully electric by 2030.* [Online]. Available: `https://www.media.volvocars.com/global/en-gb/media/pressreleases/277409/volvo-cars-to-be-fully-electric-by-2030` (visited on 03/08/2022).

[3] H. Cai, B. Guan, and L. Xu, "Low-cost ferrite pm-assisted synchronous reluctance machine for electric vehicles," *IEEE Transactions on Industrial Electronics*, vol. 61, no. 10, pp. 5741–5748, 2014. DOI: `10.1109/TIE.2014.2304702`.

[4] T. Dutta, K.-H. Kim, M. Uchimiya, *et al.*, "Global demand for rare earth resources and strategies for green mining," *Environmental Research*, vol. 150, pp. 182–190, 2016, ISSN: 0013-9351. DOI: `https://doi.org/10.1016/j.envres.2016.05.052`. [Online]. Available: `https://www.sciencedirect.com/science/article/pii/S0013935116302249`.

[5] E. A. Grunditz, S. T. Lundmark, M. Alatalo, T. Thiringer, and A. Nordelöf, "Three traction motors with different magnet materials — influence on cost, losses, vehicle performance, energy use and environmental impact," in *2018 Thirteenth International Conference on Ecological Vehicles and Renewable Energies (EVER)*, 2018, pp. 1–13. DOI: `10.1109/EVER.2018.8362387`.

[6] Z. Shao and S. Ren, "Rare-earth-free magnetically hard ferrous materials," *Nanoscale Adv.*, vol. 2, pp. 4341–4349, 10 2020. DOI: `10.1039/D0NA00519C`. [Online]. Available: `http://dx.doi.org/10.1039/D0NA00519C`.

[7] F. Byström, "Enabling circular life-cycle thinking and measuring of sustainability from an industrial ecologists perspective," 2021.

[8] E. E. Montalvo-Ortiz, S. N. Foster, J. G. Cintron-Rivera, and E. G. Strangas, "Comparison between a spoke-type pmsm and a pmasynrm using ferrite magnets," in *2013 International Electric Machines Drives Conference*, 2013, pp. 1080–1087. DOI: `10.1109/IEMDC.2013.6556230`.

[9] G. Cutuli, D. Barater, S. Nategh, and B. Raghuraman, "Aluminum hairpin solution for electrical machines in e-mobility applications. part i: Electromagnetic aspects,"

[10] T. Dimier, M. Cossale, and T. Wellerdieck, “Comparison of stator winding technologies for high-speed motors in electric propulsion systems,” in *2020 International Conference on Electrical Machines (ICEM)*, IEEE, vol. 1, 2020, pp. 2406–2412.

[11] *London metal exchange.* [Online]. Available: https://www.lme.com/ (visited on 04/01/2022).

[12] P. Pandurangan and N. Manakshya, “Permanent magnet synchronous machine using ferrite vs rare earth magnets-how do they compare?,” 2021. [Online]. Available: https://hdl.handle.net/20.500.12380/302541.

[13] M. Ibrahim, P. Sergeant, and E. Rashad, “Influence of rotor flux-barrier geometry on torque and torque ripple of permanent-magnet-assisted synchronous reluctance motors,” pp. 398–404, 2016.

[14] D. Deurell and V. Josefsson, “Fea study of proximity effect in hairpin windings of a pmsm for automotive applications,” Chalmers tekniska högskola / Institutionen för elektroteknik, 2019.

[15] T. Tokuda, M. Sanada, and S. Morimoto, “Influence of rotor structure on performance of permanent magnet assisted synchronous reluctance motor,” in *2009 International Conference on Electrical Machines and Systems*, 2009, pp. 1–6. DOI: 10.1109/ICEMS.2009.5382889.

[16] Y. Liu, J. Tang, N. Sharma, and A. Rodionov, *Electrical machines - design and analysis*, 2020.

[17] Howstuffworks. “How gear ratios work.” (2021), [Online]. Available: https://science.howstuffworks.com/transport/engines-equipment/gear-ratio.htm (visited on 02/16/2022).

[18] J. Pyrhönen, T. Jokinen, and V. Hrabovcova, *Design of Rotating Electrical Machines*, English. United Kingdom: JOHN WILEY & SONS, 2008, ISBN: 978-0-470-69516-6.

[19] TDK. “Ferrite magnets, fb series.” (2022), [Online]. Available: https://product.tdk.com/system/files/dam/doc/product/magnet/magnet/ferrite/datasheets/magnet_fb_summary_en.pdf (visited on 05/03/2022).

[20] E. A. Grunditz, *Design and assessment of battery electric vehicle powertrain, with respect to performance, energy consumption and electric motor thermal capability.* Chalmers Tekniska Hogskola (Sweden), 2016.

[21] DieselNet. “Worldwide harmonized light vehicles test cycle (wltc).” (2019), [Online]. Available: https://dieselnet.com/standards/cycles/wltp.php (visited on 02/18/2022).

[22] W. Facts. “What is wltp and how does it work?” (2021), [Online]. Available: https://www.wltpfacts.eu/what-is-wltp-how-will-it-work/ (visited on 02/18/2022).

[23] G. Kadijk, N. Ligterink, P. van Mensch, and R. Smokers, *NOx emissions of Euro 5 and Euro 6 diesel passenger cars-test results in the lab and on the road.* Delft: TNO, 2016.

[24] E. Jansson, T. Thiringer, and E. Grunditz, “Convergence of core losses in a permanent magnet machine, as function of mesh density distribution, a

case-study using finite-element analysis," *IEEE Transactions on Energy Conversion*, vol. 35, no. 3, pp. 1667–1675, 2020.

[25] *Fb9b.* [Online]. Available: `https://product.tdk.com/system/files/dam/doc/product/magnet/magnet/ferrite/catalog/magnet_fb_fb9b_en.pdf` (visited on 09/26/2021).

[26] M. Nagrial, J. Rizk, and A. Hellany, "Analysis and performance of high efficiency synchronous reluctance machines," *international journal of energy and environment*, vol. 2, no. 2, pp. 247–254, 2011.

[27] A. Ortega Dulanto, *Design of a synchronous reluctance motor assisted with permanent magnets for pump applications*, 2015.

[28] P. Mancinelli, S. Stagnitta, and A. Cavallini, "Qualification of hairpin motors insulation for automotive applications," *IEEE Transactions on Industry Applications*, vol. 53, no. 3, pp. 3110–3118, 2017. DOI: `10.1109/TIA.2016.2619670`.

[29] C. Du-Bar and O. Wallmark, "Eddy current losses in a hairpin winding for an automotive application," in *2018 XIII International Conference on Electrical Machines (ICEM)*, 2018, pp. 710–716. DOI: `10.1109/ICELMACH.2018.8507265`.

[30] A. T. Tabereaux and R. D. Peterson, "Chapter 2.5 - aluminum production," in *Treatise on Process Metallurgy*, S. Seetharaman, Ed., Boston: Elsevier, 2014, pp. 839–917, ISBN: 978-0-08-096988-6. DOI: `https://doi.org/10.1016/B978-0-08-096988-6.00023-7`. [Online]. Available: `https://www.sciencedirect.com/science/article/pii/B9780080969886000237`.

[31] A. Nordelöf, E. Grunditz, A.-M. Tillman, T. Thiringer, and M. Alatalo, "A scalable life cycle inventory of an electrical automotive traction machine–technical and methodological description," Chalmers University of Technology, Tech. Rep., 2016.

[32] E. A. Grunditz, S. T. Lundmark, M. Alatalo, T. Thiringer, and A. Nordelöf, "Three traction motors with different magnet materials—influence on cost, losses, vehicle performance, energy use and environmental impact," in *2018 thirteenth international conference on ecological vehicles and renewable energies (EVER)*, IEEE, 2018, pp. 1–13.

[33] T. Rydberg and B. Steen. "Environmental priority strategies in product design (eps)." (2022), [Online]. Available: `https://www.lifecyclecenter.se/projects/environmental-priority-strategies-in-product-design-eps/` (visited on 04/08/2022).

[34] T. Rydberg, *Eps weighting factors-version 2020d*, 2020. (visited on 04/01/2022).

[35] J. Dai, Y. Dai, Z. Wang, and H. Gao, "Preparation and magnetic properties of lanthanum-and cobalt-codoped m-type strontium ferrite nanofibres," *Journal of Experimental Nanoscience*, vol. 10, no. 4, pp. 249–257, 2015.

[36] U. S. E. P. Agency. "Understanding global warming potentials." (2021), [Online]. Available: `https://www.epa.gov/ghgemissions/understanding-global-warming-potentials` (visited on 04/12/2022).

[37] A. Nordelöf, E. Grunditz, S. Lundmark, A.-M. Tillman, M. Alatalo, and T. Thiringer, "Life cycle assessment of permanent magnet electric traction motors," *Transportation Research Part D: Transport and Environment*, vol. 67, pp. 263–274, 2019.

[38] P. Nuss and M. J. Eckelman, "Life cycle assessment of metals: A scientific synthesis," *PloS one*, vol. 9, no. 7, e101298, 2014.

[39] H. Stratosphere. "What is silicon steel?" (2021), [Online]. Available: `https://www.homestratosphere.com/what-is-silicon-steel/` (visited on 05/04/2022).

[40] *Smm rare earth metals*. [Online]. Available: `https://www.metal.com/Rare-Earth-Metals` (visited on 04/01/2022).

[41] *Detailed export data of electrolytic iron powder*. [Online]. Available: `https://www.zauba.com/export-electrolytic-iron-powder-hs-code.html` (visited on 04/12/2022).

[42] *Detailed export data of boron*. [Online]. Available: `https://www.zauba.com/export-boron-hs-code.html` (visited on 04/12/2022).

[43] *Minerals yearbook 2020 tables-only release*. [Online]. Available: `https://www.usgs.gov/centers/national-minerals-information-center/strontium-statistics-and-information` (visited on 04/01/2022).

[44] *Study of a permanent magnet motor with maxwell 2d: Example of the 2004 prius ipm motor*. [Online]. Available: `https://forum.ansys.com/61510114-Study-of-a-permanent-magnet-motor-with-maxwell-2d-example-of-the-2004-prius-ipm-motor.html` (visited on 01/31/2022).

A

Material specification

A.1 Copper

The material properties for copper was obtained from SysLibrary in Ansys Electronics and is presented in Table A.1.

Table A.1: Properties of copper.

Property	Value	Unit
Relative permeability	0.999991	
Bulk conductivity	58	MSiemens/m
Mass density	8933	kg/m^3
Young's modulus	120	GN/m^2
Poisson's Ratio	0.38	

A.2 Nd(Dy)FeB

The material properties for the Nd(Dy)FeB magnets were obtained from the reference model and are presented in Table A.2.

Table A.2: Properties of Nd(Dy)FeB.

Property	Value	Unit
Coercive Force, H_c	-849.2	kA/m
Residual magnetic flux density, B_r	1.15	T
Relative permeability	1.08	
Bulk conductivity	0.67	MSiemens/m
Young's modulus	200	GN/m^2

A.3 M19_29G Electrical Steel

The material properties for the core material, M19_29G, was obtained from [44], and is presented in Table A.3. Further, the data for the BH curve is presented in

Table A.4 and the core loss as a function of flux density and the frequency is shown in Table A.5.

Table A.3: Properties of M19_29G.

Property	Value	Unit
Core loss model	Electrical steel	W/m^3
Kh	184.234	
Kc	0.386	
Ke	0.270	
Mass density	7872	kg/m^3

Table A.4: BH table of M19_29G.

H (A/m)	B (T)
0	0
22.28	0.05
25.46	0.1
31.83	0.15
47.47	0.36
63.66	0.54
79.57	0.65
159.15	0.99
318.3	1.2
477.46	1.28
636.61	1.33
795.77	1.36
1591.5	1.44
3183	1.52
4774.6	1.58
6366.1	1.63
7957.7	1.67
15915	1.8
31830	1.9
111407	2
190984	2.1
350138	2.3
509252	2.5
560177.2	2.56
1527756	3.78

Table A.5: Core loss versus frequency of M19_29G.

B (T)	P (W)				
	50 Hz	100 Hz	200 Hz	400 Hz	1000 Hz
0	0	0	0	0	0
0.1	0.03	0.04	0.09	0.21	0.99
0.2	0.07	0.16	0.37	0.92	3.67
0.3	0.13	0.34	0.79	1.99	7.63
0.4	0.22	0.55	1.31	3.33	12.7
0.5	0.31	0.8	1.91	4.94	18.9
0.6	0.43	1.08	2.61	6.84	26.4
0.7	0.54	1.38	3.39	9	35.4
0.8	0.68	1.73	4.26	11.4	46
0.9	0.83	2.1	5.23	14.2	58.4
1	1.01	2.51	6.3	17.3	73
1.1	1.2	2.98	7.51	20.9	90.1
1.2	1.42	3.51	8.88	24.9	-
1.3	1.7	4.15	10.5	29.5	-
1.4	2.12	4.97	12.5	35.4	-
1.5	2.47	5.92	14.9	41.8	-
1.6	2.8	-	-	-	-
1.7	3.05	-	-	-	-
1.8	3.25	-	-	-	-

A.4 FB9B

The material properties for the FB9B ferrite magnets was obtained from the supplier TDK [25], and is presented in Table A.6.

Table A.6: Properties of FB9B.

Property	Value	Unit
Coercive Force, H_c	342.2	kA/m
Residual magnetic flux density, B_r	0.45	T
Relative permeability	1.05	
Bulk conductivity	1.5	MSiemens/m
Young's modulus	200	GN/m^2

A.5 Aluminium

The material properties for aluminium was obtained from SysLibrary in Ansys Electronics and is presented in Table A.7.

Table A.7: Properties of aluminium.

Property	Value	Unit
Relative permeability	1.000021	
Bulk conductivity	38	MSiemens/m
Mass density	2689	kg/m^3
Young's modulus	69	GN/m^2
Poisson's Ratio	0.31	

DEPARTMENT OF ELECTRICAL ENGINEERING
CHALMERS UNIVERSITY OF TECHNOLOGY
Gothenburg, Sweden
www.chalmers.se

CHALMERS
UNIVERSITY OF TECHNOLOGY